Precambrian Research 316 (2018) 103–126

Contents lists available at ScienceDirect

Precambrian Research

journal homepage: www.elsevier.com/locate/precamres

Protracted zircon geochronological record of UHT garnet-free granulites in the Southern Brasília orogen (SE Brazil): Petrochronological constraints on magmatism and metamorphism

Mahyra Tedeschi[a,b,*], Antonio Pedrosa-Soares[a,1], Ivo Dussin[a,c,1], Pierre Lanari[d], Tiago Novo[a], Marco Aurélio P. Pinheiro[b], Cristiano Lana[e,1], Daniel Peters[f]

[a] Programa de Pós-Graduação em Geologia, Universidade Federal de Minas Gerais, IGC-CPMTC, Av. Antônio Carlos 6627, Belo Horizonte, Brazil
[b] Geological Survey of Brazil (CPRM), Avenida Brasil 1731, Belo Horizonte, MG, Brazil
[c] Faculdade de Geologia, Universidade do Estado do Rio de Janeiro, R. São Francisco Xavier 524, Rio de Janeiro, Brazil
[d] Institute of Geological Sciences, University of Bern, Baltzerstrasse 1-3, Bern, Switzerland
[e] Laboratório de Geoquímica Isotópica, Universidade Federal de Ouro Preto, Campus Morro do Cruzeiro, Ouro Preto, Brazil
[f] Institut de Recherche en Astrophysique et Planétologie (IRAP), Observatoire Midi-Pyrénées (OMP), CNRS, 14 avenue Edouard Belin, 31400 Toulouse, France

ARTICLE INFO

Keywords:
Protracted zircon geochronological record
Petrochronology
UHT metamorphism
Paranapanema block
Guaxupé nappe
Brasília orogen

ABSTRACT

The investigation of ultrahigh temperature (UH*T*) metamorphic rocks, and their corresponding (pressure)-temperature-time (*P*-*T*-t) history is critical to distinguish between arc- or collision-related metamorphism. This is a very challenging task if mineral assemblages are highly retrogressed and isotopic systems are disturbed. Garnet-free granulites lacking accessory minerals (chronometers) and metamorphic index minerals (thermobarometers) located in UHT domains are examples of such complex systems. In such cases, zircon may be the main chronometer, although isotopic U-Pb data outline protracted records, making the interpretation of the data complex. This study focuses on the timing of magmatism and metamorphism, as well as on the thermal metamorphic conditions of garnet-free UHT granulites of the Guaxupé nappe, southernmost Brasília orogen, located close to the Paranapanema cratonic block. It presents U-Pb dating, Lu-Hf isotopes and trace element signatures of zircon, and thermometry on metamorphic clinopyroxene and orthopyroxene from granulites. Steady $^{176}Hf/^{177}Hf_{(t)}$ in zircon cores exhibiting U-Pb dates spreading in the Concordia suggest post-crystallization disturbance. From those disturbed granulitic systems, minimum crystallization ages of ca. 2550 Ma, ca. 790 Ma, ca. 690 Ma and ca. 660 Ma can be retrieved. The juvenile ca. 2.55 Ga granulite is the first evidence of an exposed rock of the Paranapanema cratonic block, previously only inferred from geophysical data. The Guaxupé nappe records arc-related magmatic episodes in the range of 790–640 Ma, partially coeval with a long-lasting (~80 m.y.) metamorphic event (670–590 Ma) and intrusion of basic magma (ca. 660 Ma). Thermometry on zoned clinopyroxene and orthopyroxene yields UHT conditions around 900–1000 °C. Comparing the distribution patterns of metamorphic zircon rims and newly formed grains, we suggest two distinct metamorphic stages: i) an arc-related metamorphism (670–640 Ma), recorded by domains possibly formed by subsolidus recrystallization; and ii) a continental collision to decompression involving partial melting (630–590 Ma) associated to extensive zircon crystallization. The temporal relationship between magmatic and metamorphic ages suggests an ultra-high-temperature metamorphic event related to a magmatic arc. This arc was afterwards involved by the Guaxupé nappe stacking during the collisional stage of the southernmost Brasília orogen.

1. Introduction

Identifying protoliths and reconstructing the metamorphic history of rocks that experienced ultrahigh-temperature (UH*T*) metamorphism is particularly challenging. This type of metamorphism can affect both the appearance and the composition of a rock due to major mineral reactions, overstepping elemental and isotopic closure temperatures and open system behavior. Partial melting and melt extraction are known to fractionate chemical components, and variably reset isotopic systems (Kelsey and Hand, 2015; Taylor et al., 2016). The estimation of

* Corresponding author.
E-mail address: mahyratedeschi@gmail.com (M. Tedeschi).
[1] Fellow of the Brazilian Research Council (CNPq).

https://doi.org/10.1016/j.precamres.2018.07.023
Received 19 December 2017; Received in revised form 19 July 2018; Accepted 31 July 2018
Available online 01 August 2018

metamorphic conditions, rates and durations of such processes (i.e., *T-t* and *P-T-t* paths) are crucial. They can provide valuable insights on the tectonic settings and causes of UH*T* metamorphism (Harley, 2016; Kelsey, 2008; Kelsey and Hand, 2015). They may also help to unravel pre-metamorphic processes (Kemp et al., 2007; Möller et al., 2003; Stepanov et al., 2016).

Geochronometers are pivotal for the investigation of tectonometamorphic processes, as they permit to constrain their duration and rate. Notwithstanding, even zircon, generally regard as a robust accessory mineral with high U/Pb closure temperature (> 900 °C; e.g., Cherniak, 2010), can lose its time records under UH*T* conditions (Cherniak and Watson, 2003). Examples of both preserved (Drüppel et al., 2013; Ewing et al., 2013; Möller et al., 2003) and variably reseted ages (Stepanov et al., 2016; Wang et al., 2017) have been described for H*T* to UH*T* terranes. A common outcome is the protracted spreading of U-Pb zircon data along the Concordia or outlining a sub-parallel Discordia line (Vervoort and Kemp, 2016; Wang et al., 2017; Wasserburg, 1963; Whitehouse and Kemp, 2010). The spread of zircon ages may also suggest long-lasting metamorphic events with episodic zircon growth and/or partial resetting (Laurent et al., 2018; Rubatto, 2017; Taylor et al., 2016; Vervoort and Kemp, 2016). The interpretation of this age record is therefore complex and challenging.

The original protolith composition and subsequent melt and fluid-rock interactions affect the stable mineral assemblage used to retrieve *P-T-t* information (Carrington and Harley, 1995; Rubatto, 2017; Taylor et al., 2016). Partial melting, involving incongruent reactions and interaction between melts and fluids, can add further complexity to these already challenging complex local bulk systems (e.g., Lanari and Engi, 2017). Temperature – and also pressure – conditions are commonly obtained from Mg- and Al-rich rocks, which can contain unequivocal UH*T* mineral assemblages such as sapphirine + quartz (e.g., Baldwin et al., 2005; Harley, 1998; Kelsey et al., 2004; Santosh et al., 2007) or orthopyroxene + sillimanite ± quartz (e.g., Kelly and Harley, 2004; Moraes and Fuck, 2000). Less attention has been paid to associated garnet-free mafic granulites, which lack diagnostic UH*T* assemblages. In such context, the UH*T* conditions are often inferred based on thermobarometry applied to the associated rocks (Kelsey, 2008; Kelsey and Hand, 2015). Mafic granulites contain pyroxene that is usually interpreted to have an igneous origin, preventing the use of pyroxene-thermometry unless garnet is also present (Kelsey, 2008). Recently, Yang and Wei (2017) showed that major element-based thermometers for mafic granulites may underestimate the predicted temperatures compared to REE-based thermometers (Liang et al., 2013; Sun and Liang, 2015), especially for garnet-free clinopyroxene-orthopyroxene granulites. This was attributed to the partial resetting of Fe-Mg exchange thermometers by diffusion (Bègin and Pattison, 1994). In addition, basic rock compositions do not favor the crystallization of accessory minerals such as monazite and allanite, which can play an important role since these can be used to derive time and link ages to temperature constraints (Engi, 2017).

In order to solve these problems, different strategies have been developed and employed. Concerning the interpretation of complex U-Pb data, an examination and description of the full range of age data is critical if one wants to retrieve the duration and thermal intensity of metamorphism (Taylor et al., 2016). Coupling between U-Pb and Lu-Hf analyses in zircon have proven to be an efficient tool to enhance understanding of the data spread in the Concordia (Vervoort and Kemp, 2016; Wang et al., 2017; Whitehouse and Kemp, 2010). Hf isotopic data also provide petrogenetic information of rocks that experienced geochemical changes during high-grade metamorphism (i.e. migmatization or interaction with fluids), even in metasedimentary rocks (Belousova et al., 2002; Kemp et al., 2007). Metamorphic temperatures of unfavorable assemblages obtained with Ti-in-zircon and clinopyroxene-orthopyroxene thermometry may represent at least minimum estimates (Kelsey and Hand, 2015; Taylor et al., 2016; Yang and Wei, 2017).

The complexity of such petrochronological investigations partly explains why the *P-T-t* conditions of garnet-free granulites from the Guaxupé nappe, Southern Brasília orogen (southeastern Brazil), have remained mostly unknown. The Guaxupé nappe comprises metamorphic remnants of a Neoproterozoic magmatic arc and associated supracrustal rocks (Campos Neto and Caby, 1999, 2000; Campos Neto et al., 2011), including UH*T* garnet-bearing granulites and migmatites recording temperatures up to 1000 °C (Del Lama et al., 2000; Rocha et al., 2017, 2018). U-Pb zircon data (TIMS, LA-ICP-MS) from both the granulites and their melting products have provided continuous concordant age records, spreading for more than 100 Ma and interpreted based on number clusters (Mora et al., 2014; Reno et al., 2009; Rocha et al., 2017, 2018).

Our study focuses on processes and timing involved in the generation and evolution of a series of mafic to intermediate rocks. The garnet-free granulites of the Guaxupé nappe were investigated by combining U-Pb geochronology, Lu-Hf and trace element analyses in zircon, together with quantitative compositional mapping, conventional thermobarometry, and Ti-in-zircon thermometry. This multi-method approach provides a solid basis to decipher the magmatic and metamorphic histories of the UH*T* garnet-free granulites and associated rocks, and bring further constraints to the evolution of the Southern Brasília orogen.

2. Geological setting

2.1. General framework

The Brasília orogenic system is an 1800 km-long, boomerang-shaped, nearly N-S trending belt (Fig. 1A), formed during Western Gondwana amalgamation in the Neoproterozoic (Brito Neves et al., 1999; Cordani et al., 2003). The northern and southern segments of the Brasília system evolved separately during the Brasiliano orogenic event, representing distinct collision zones against the northwest and southwest margins of the São Francisco craton (Valeriano, 2017). The Southern Brasília orogen resulted from the convergence and collision between the Paranapanema (active margin) and São Francisco (passive margin) paleocontinental blocks at around 630 Ma (Campos Neto et al., 2011; Coelho et al., 2017; Mantovani and Brito-Neves, 2005, 2009; Trouw et al., 2013). A complex framework of east-verging nappe systems developed during the collisional stage (Campos Neto and Caby, 1999, 2000; Campos Neto et al., 2011; Trouw et al., 2000, 2013; Valeriano, 2017). Each nappe system comprises specific geotectonic components with distinctive tectono-metamorphic domains (Fig. 1B, C and 2).

The migmatized granulite and amphibolite facies rocks (Fig. 1B and 2) from the Socorro-Guaxupé nappe system (SGN) includes remnants of Neoproterozoic magmatic arc and associated sedimentary units that were thrusted over the metasedimentary rocks of the Andrelândia nappe system (Campos Neto and Figueiredo 1995; Campos Neto et al., 2011; Trouw et al., 2013). The Ouro Fino shear zone splits the Socorro-Guaxupé nappe system into two lobes, the Guaxupé nappe (GN), focus of the present paper, and the Socorro nappe (Trouw et al., 2013). It has been suggested that rocks from the Guaxupé nappe constitute an extension of the Goiás magmatic arc, which started developing in central-northern segments of the Brasília orogen around 800–850 Ma (e.g., Pimentel and Fuck, 1992; Pimentel et al., 2000). However, similar crystallization ages around 800 Ma, as well as juvenile Lu-Hf and Sm-Nd signatures, were not hitherto found in the Guaxupé nappe (Janasi, 1999; Mora et al., 2014; Rocha et al., 2017, 2018). An age of ca. 800 Ma reported for an orthogneiss from the Embu Complex (Cordani et al., 2002), to the southeast, was interpreted as part of the Socorro-Guaxupé nappe by some authors (e.g., Trouw et al., 2013; Vinagre et al., 2017).

Although the Paranapanema block (Mantovani and Brito-Neves, 2005, 2009) has been envisaged as basement of the Guaxupé nappe (Campos Neto et al., 2011; Trouw et al., 2013), it is assumed to be completely covered by the Paraná basin and to not crop out at the

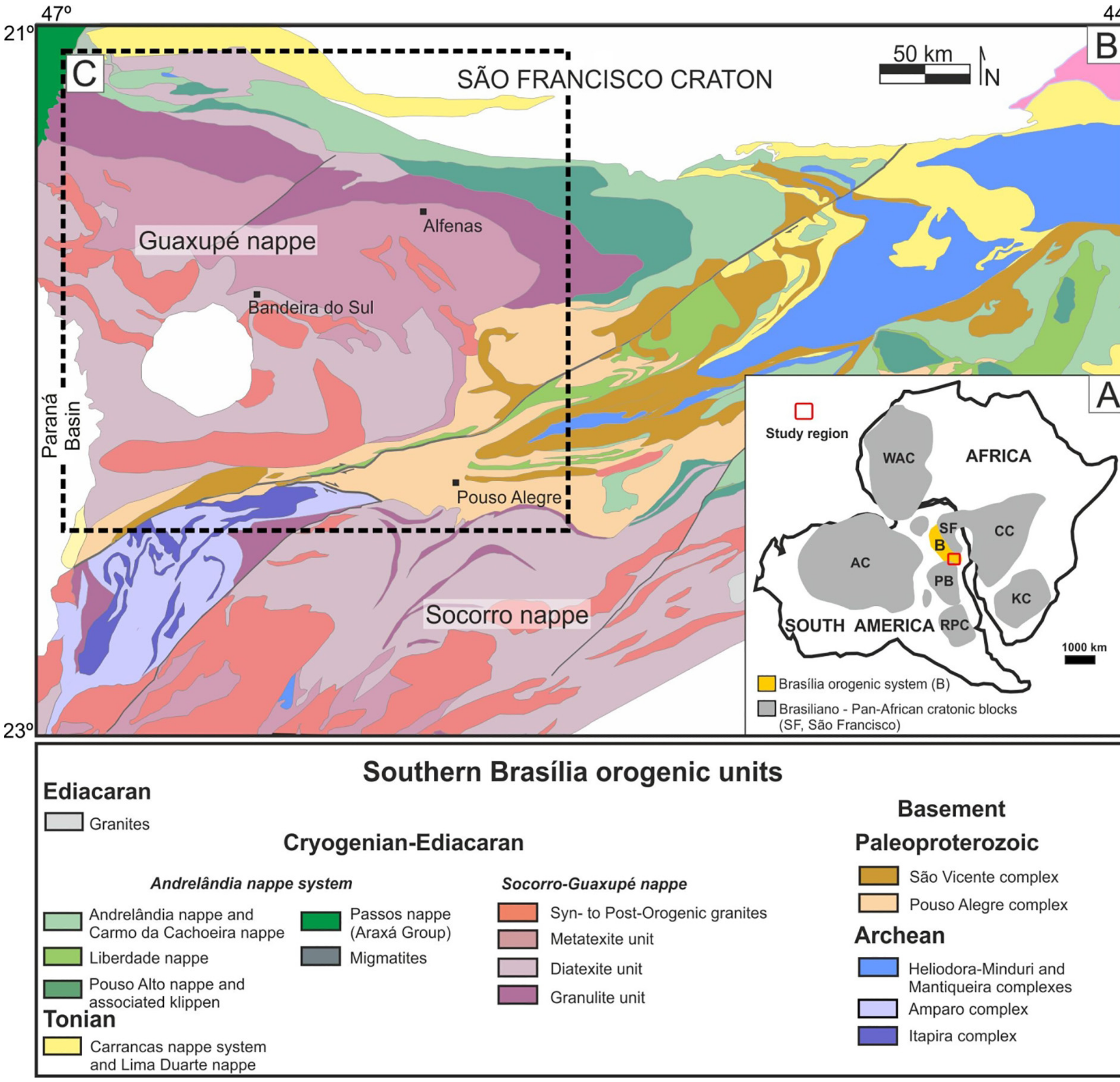

Fig. 1. (A) Distribution of cratonic blocks and orogens in Western Gondwana (red rectangle: location of the studied region illustrated in B): WAC, West African craton; AC, Amazonian craton; SF, São Francisco craton; CC, Congo craton; PB, Paranapanema block; KC, Kalahari craton; RPC, Rio de la Plata craton. (B) Sketch map of the southernmost Brasília orogen (modified from Campos Neto et al., 2011; Cioffi et al., 2016a; Westin et al., 2016). (C) Dashed rectangle shows the location of the geological map displayed in Fig. 2. (For interpretation of the references to color in this figure legend, the reader is referred to the web version of this article.)

surface (Fig. 1). The existence of this block was inferred from ancient granitic rocks recovered by drilling beneath the Paraná basin (Cordani et al., 1984), regional geophysical data and geochemical fingerprints from Cretaceous basalts (Mantovani and Brito-Neves, 2005, 2009). Paleoproterozoic U-Pb ages (ca. 2.1 Ga) from gneisses of the Socorro nappe were suggested to represent part of the block (Trouw, 2008). Our data presented in the following provide the first evidence of exposure within the Guaxupé nappe of rocks belonging to the Paranapanema block.

2.2. The Guaxupé nappe

The Guaxupé nappe has been divided by Campos Neto and Caby (2000) into three regional rock-assemblages called: the granulitic, diatexitic and metatexitic units (Fig. 1B). In detail, however, rocks from all these "units" can be found together in the same outcrop, forming individual lithotypes one within each other (Rocha et al., 2017), or within tectonic slices and plutons (Tedeschi et al., 2015).

The granulitic unit roughly correlates with the Elói Mendes unit (Fig. 2). It occurs at the base of the Guaxupé nappe, and as tectonic slices enveloped by migmatites of the São João da Mata unit (Tedeschi et al., 2015). The Elói Mendes unit mainly comprises banded, felsic to mafic, (garnet)-orthopyroxene-clinopyroxene-bearing granulites, with charnockitic to enderbitic leucosomes roughly parallel to the regional foliation and cut by veins and patches of pink hornblende-bearing granite (Campos Neto and Caby, 2000; Mora et al., 2014; Rocha et al., 2017; Tedeschi et al., 2015). These authors suggest that the charnockitic to enderbitic leucosomes are product of autochthonous anhydrous anatexis.

The metatexitic and diatexitic units roughly correspond to the São João da Mata unit (Fig. 2). It mainly consists of (orthopyroxene)-(hornblende)-biotite and (orthopyroxene)-(garnet)-biotite migmatites, and minor metasedimentary rocks (e.g., kinzigite, schist, quartzite; Campos Neto and Caby, 2000; Ribeiro et al., 2015a; Rocha et al., 2017; Tedeschi et al., 2017). The São João da Mata unit shows a north-to-south increase in the degree of anatexis (Campos Neto and Caby, 2000; Tedeschi et al., 2015) from predominantly metatexites, to the north of Botelhos city (Fig. 2), to mostly diatexites towards Bandeira do Sul city

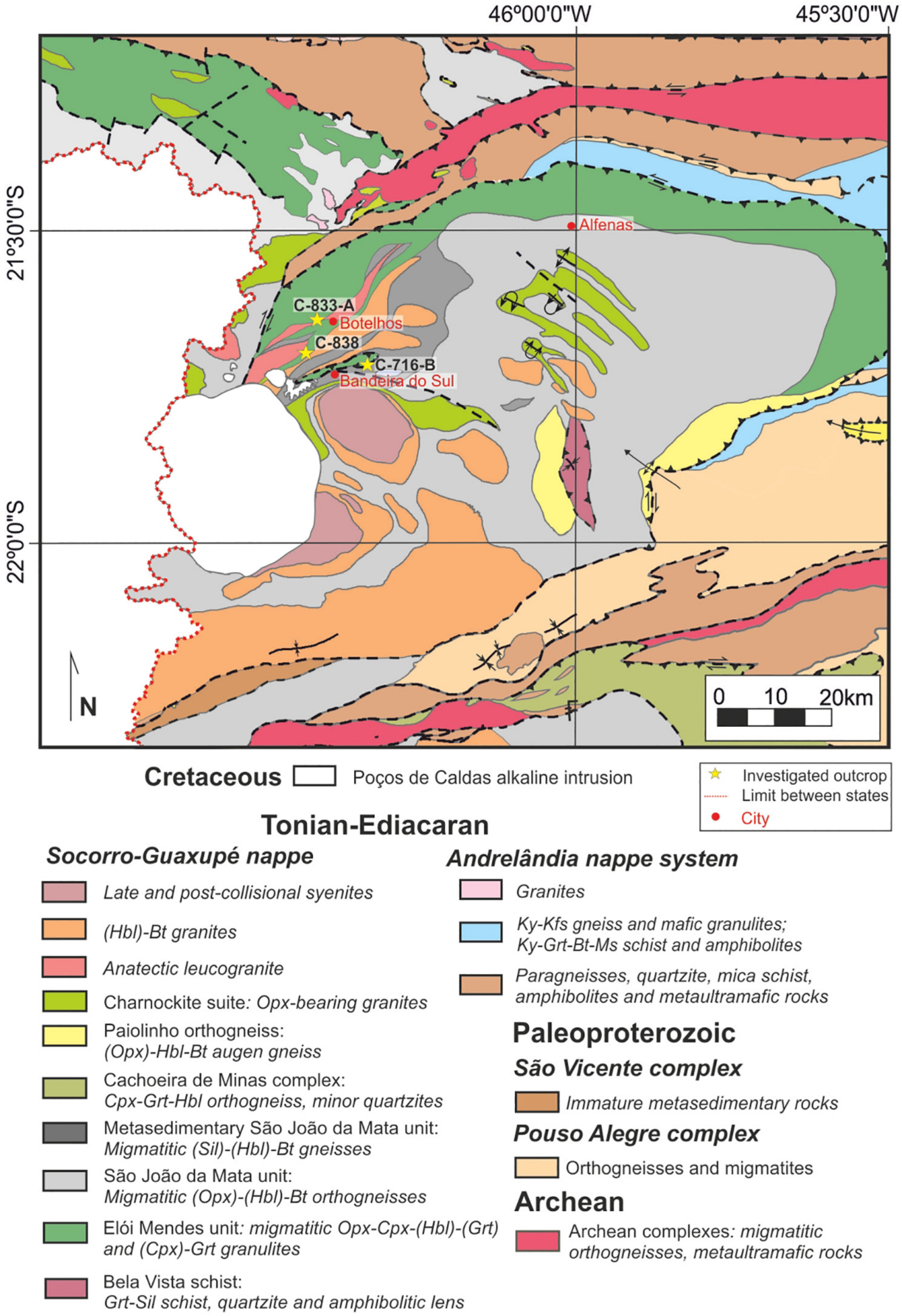

Fig. 2. Regional geological map of the Guaxupé nappe showing the location of investigated outcrops (yellow stars). Map compiled and simplified from Degler et al. (2015); Zogheib et al. (2015); Peixoto et al. (2015); Ribeiro et al. (2015a, b, c); and Tedeschi et al. (2015); with inputs from Cioffi et al. (2016a) and Westin et al. (2016). Dotted red line indicates the boundary between Minas Gerais (east) and São Paulo (west) states. (For interpretation of the references to color in this figure legend, the reader is referred to the web version of this article.)

(Campos Neto and Caby, 2000; Tedeschi et al., 2015).

The Guaxupé nappe, formed during the collisional event of the Southern Brasília orogen, comprises remains of a pre-collisional magmatic arc formed on an active continental margin from ca. 730 to ca. 640 Ma (Campos Neto and Figueiredo, 1995; Campos Neto and Caby, 2000; Hackspacher et al., 2003; Mora et al., 2014; Rocha et al., 2018). Clusters of concordant U-Pb ages suggest a main period of pre-collisional magmatism around 655–650 Ma (Rocha, 2016). These rocks later experienced UH*T* metamorphism at 630–625 Ma (Rocha et al., 2017). Ages around 610 Ma from soccer-ball zircons have been attributed to a retrograde cooling stage (Mora et al., 2014) and post-collisional emplacement of syenitic bodies (Töpfner, 1996). Conventional thermobarometry applied to orthopyroxene-garnet granulites provided peak *P-T* conditions of 900 °C at 12 kbar (Rocha et al., 2018) and 1040 °C at 14 kbar (Del Lama et al., 2000) for the granulitic unit. These P-T conditions have either been attributed to metamorphism in the deep root of a magmatic arc (Campos Neto and Caby, 2000; Campos Neto et al., 2004), or to collisional crustal thickening associated with minor mafic magma underplating (Rocha, 2016). Peak *P-T* conditions of 1030 °C at 11.7 kbar were obtained from paraderived garnet-orthopyroxene

Table 1
Summarized details of the studied samples. UTM coordinates are relative to the WGS84 datum. Minimum crystallization ages (see text for explanation); 1-Temperature outliers; 2-Concordia age; *Data based on inherited grain (see text for details); εHf calculated for grain individual $^{207}Pb/^{206}Pb$ dates (t).

Sample	Rock	UTM Coordinates		Mineral assemblage		Protolith			Metamorphism		T-(P) conditions			
		E	N	Major	Minor	Minimum crystallization age (Ma)	εHf	Ti-in- zircon T (°C)	Data range (Ma)	εHf(t)	Ti-in-zircon T (°C)	T Peak (°C)	T Retrog. (R1) (°C)	T and P Retrog. (R2) (°C and kbar)
C-833-A	banded granulite	354,420	7,605,627	Hbl + Opx + Cpx + Pl + Kfs + Bt + Qz	Ilm + Ap + Zrn + Py	2559 ± 66	+2.72 to +10.0	~ 695–840 *990; 1025 and ~1150*[1]	2405 ± 10[2] ~590–680	n.a. -18.5 to −34.7	~590–715 ~680–740 *~878 and ~1135*[1]	n.a.	n.a.	n.a
C-838-2	opdalite	352,305	7,600,153	Opx + Cpx + Hbl + Pl + Kfs + Bt + Qz	Zrn + Ap + Rt + Ilm	786 ± 10	−11.8 to −15.8	670–780	~630–690	−12.6 to −13.4	~690–700	998 ± 23	865 ± 38	740 ± 28 and ~6
C-838-A	banded granulite	352,305	7,600,153	Hbl + Opx + Cpx + Pl + Kfs + Bt + Qz	Ilm + Ap + Zrn	691 ± 3	−8.2 to −12.6	~690–780 *~920*[1]	~570–670	-9.0 to −14.1	~700–830	n.a.	n.a.	n.a.
C-838-B	Hbl-Bt granitic leucosome	352,305	7,600,153	Bt + Pl + Kfs + Qz + Hbl	Rt + Ilm + Zrn + Py	2.7 Ga*	-3.7*	n.a.	~580–680	−20.9 to −52.1	n.a.	n.a.	n.a.	n.a.
C-716-B	mafic granulite enclave	361,224	7,597,330	Opx + Cpx + Hbl + Pl + Bt	Ilm + Mag + Py + Ccp + Zrn + Qz + Ap	664 ± 9	−5.9 to −11.4	~710–810 *1010*[1]	n.a.	n.a.	n.a.	n.a.	n.a.	n.a.

migmatites of the metatexitic unit (Rocha et al., 2017).

3. Sampling and field relationship

Five rock samples were collected from large and fresh outcrops of the granulitic unit, exposed in roadcuts of the BR-146 and BR-267 highways (Fig. 2; location details are given in Table 1). Along a NW-SE 15 km section, granulites of the Elói Mendes unit crop out either in the sheared outer border of the granulitic wedge or as a tectonic slice enveloped by the diatexitic São João da Mata unit (Figs. 2 and 3). The outcrops reveal a transitional migmatitic granulite with stromatic metatexites to schollen diatexites prevailing in the northern segment of the section. To the south, schollen to nebulitic diatexites are the most common migmatitic structures (Fig. 3).

The stromatic metatexite consists of mm- to cm-thick sharp-layered migmatite (Fig. 3C and F). This greenish banded granulite shows melanocratic to mesocratic (dark green) fine-grained bands alternating with light green medium-grained bands representing leucosomes (Fig. 3B, C and F). The felsic bands exhibit coarse-grained peritectic orthopyroxene, clinopyroxene and/or hornblende (Fig. 3C, D and H). At the mesoscopic scale, from the bottom to the top of the outcrop, a progressive increase of the volume of light green medium-grained leucosome is observed (sketch in Fig. 3).

On the top, where leucosome fractions prevail (Fig. 3), centimetric to up to 2 m long schollen characterize the diatexite. These include light-green enderbitic to charnockitic leucosomes, and pink to light gray hornblende-biotite-bearing leucosomes (sample C-838-B). On the whole, the schollen diatexite contains (Fig. 3A): i) fine-grained mafic granulite or amphibolite (#1 in Fig. 3A), representing the residue (#1 in Fig. 3D); ii) banded granulite with bands of orthopyroxene-bearing leucosome; iii (#2 in Fig. 3A and F; samples C-833-A and C-838-A); iii) light green enderbitic, opdalitic and charnockitic leucosomes (#3 and #4 in Fig. 3); and iv) pink to light gray hornblende-biotite-bearing leucosomes (#5 in Fig. 3A and E; sample C-838-B).

Both metatexites and diatexites display leucosome bands and lodes parallel to folds and foliation, which can be cross cut by mm- to m-thick veins. Those leucosomes seem to be *in situ* and *in source* partial melting products. They connect with metric to decametric veins and irregular-shaped bodies of light green orthopyroxene-bearing rocks, showing faint transitions from the stromatic metatexite to the enderbitic to charnockitic leucosomes. All those features suggest feeding relationships from melt sources and storage batches. Locally, the light-green charnockitic rocks cut and enclose enclaves of mafic granulite, depicting a breccia-like structure of more intricate origin (Fig. 3 and B; sample C-833-A). This type of structure suggests that part of the light green enderbitic to charnockitic rocks represent allochthonous melts, crystallized as intrusive bodies, not necessarily corresponding to *in source* leucosomes. Nonetheless, the parental rocks, i.e., the melt source, seems to be deeper parts of the same source of the similar leucosomes.

The pink to light gray hornblende-biotite granitic leucosomes often cut the host metatexite, exhibiting either sharp or faint transitions to the green leucosomes and suggesting local mixing of melts. Where the rock preserves a gneissic structure, centimetric to decimetric, amphibolite intercalations parallel to the banding occur.

The nebulitic diatexite consists of medium- to coarse-grained white granite, forming neosomes, usually with coarse-grained euhedral hornblende of peritectic nature (Fig. 3H), and some schlieren and schollen structures. Enclaves of fine-grained mafic granulite have a gabbroic composition (#6 in Fig. 3G; sample C-716-B). These enclaves are cut by dykes and veins of charnockitic to white hornblende-bearing leucosomes, resembling magmatic breccia (Fig. 3G). Leucosomes show a greenish-greyish color in contact with the mafic enclaves.

4. Petrography and mineral composition

The full mineral chemical dataset for samples C-833-A, C-838-A and

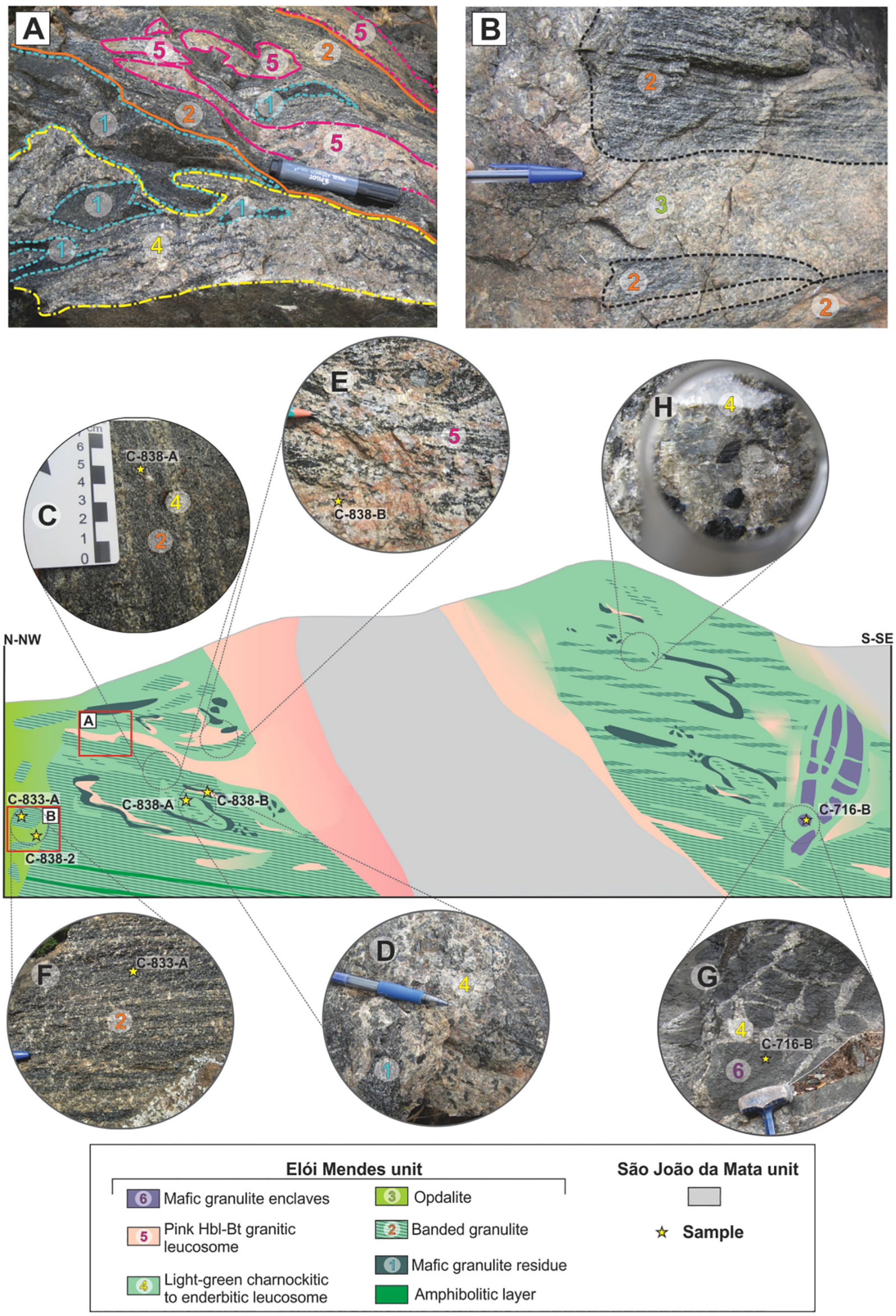

Fig. 3. Sketch cross-section showing the field relationships of the studied rocks of the granulitic – Elói Mendes unit: (1) mafic granulite (residue), (2) banded granulite, (3) opdalite, (4) light-green charnockitic to enderbitic leucosome, and (5) pink hornblende-biotite-bearing granitic leucosome, and (6) mafic granulite enclave. (A) Schollen diatexite from the northern part of the section. (B) Light-green opdalitic rock with enclaves of banded granulite. Mesoscopic aspects of each sample: (C) Banded granulite with concordant light green charnockitic leucosome in stromatic structure (C-838-A); (D) mafic schollen (residue) in charnockitic leucosome with peritectic orthopyroxene and clinopyroxene (C-838-2); (E) schlieren of biotite and schollen of stromatic metatexite in the pink hornblende-biotite-bearing granitic leucosome (C-838-B); (F) banded granulite (C-833-A); (G) Agmatic structure formed by the mafic granulite enclaves (sample C-716-B) in the diatexite; and (H) euhedral peritectic hornblende in the nebulitic diatexite. (For interpretation of the references to color in this figure legend, the reader is referred to the web version of this article.)

C-838-B is tabulated in supplementary materials S1, S3 and S4. The compositional map is provided for sample C-838-A. The analytical procedures are described in Appendix A. Mineral abbreviations are from Whitney and Evans (2010).

4.1. Banded granulite (C-833-A)

The banded granulite (C-833-A) consists of alternating bands of dark green fine-grained granulites (residue) and light green charnockitic leucosomes, with faint contacts between the bands (Figs. 4A and 5B). The dark green fine-grained bands exhibit granonematoblastic texture, and are composed of clinopyroxene (5–10 vol%), orthopyroxene (5–8%), oligoclase-andesine (50–60%) and quartz (5%), with retrograde hornblende (15–20%) and biotite (10–15%). The light green charnockitic leucosome shows granoblastic texture, and consists of oligoclase (80 vol%), quartz (10%) and mafic minerals (orthopyroxene + clinopyroxene + hornblende = 10%). A regional foliation is defined by oriented mafic minerals in mafic bands, and quartz ribbons in leucosomes. Quartz usually shows chessboard extinction. Ilmenite, apatite, zircon and pyrite are accessory minerals.

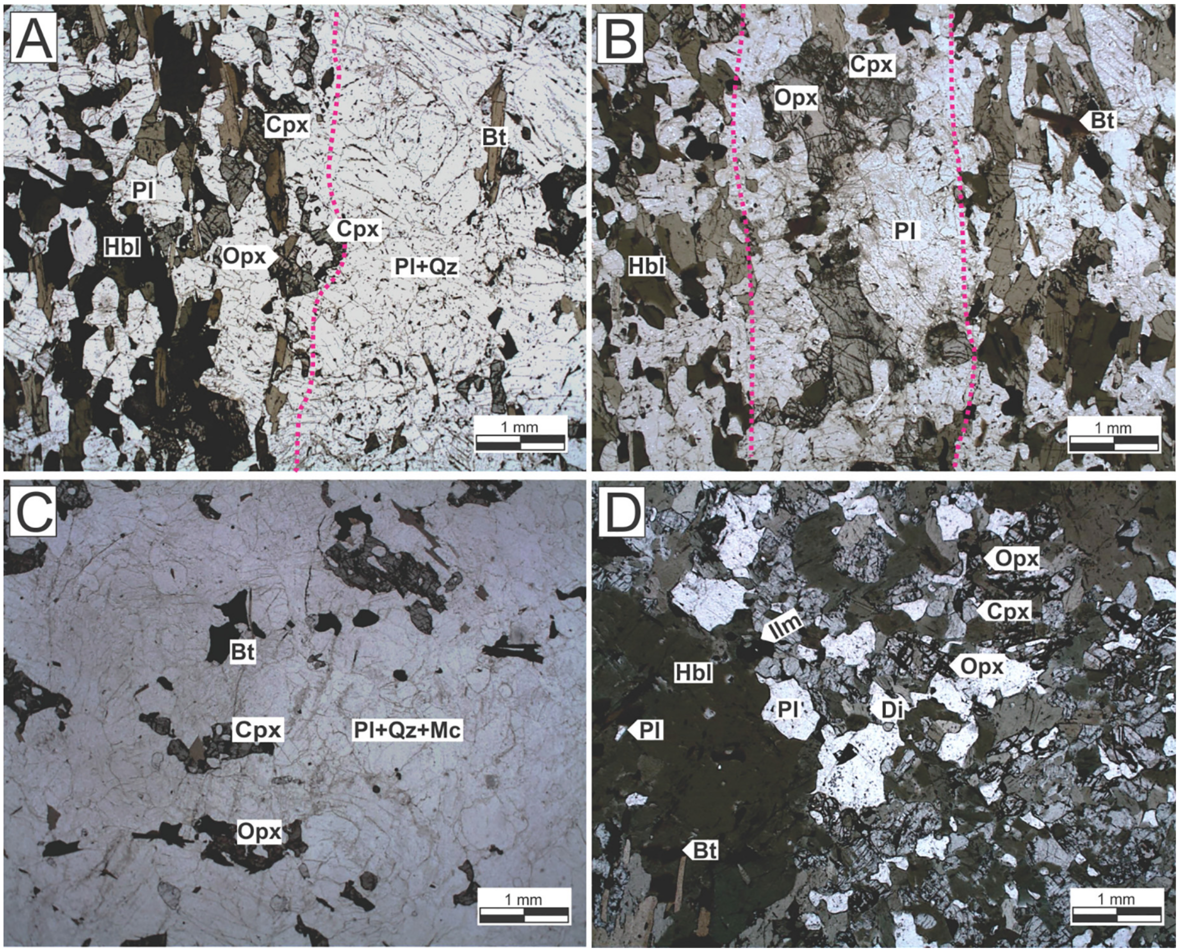

Fig. 4. Transmitted light, non-polarized photomicrographs from the studied rocks. Dotted pink lines outline faded domanial boundaries between leucosome and residue. (A) Relation between thin bands of residue and leucosome in the banded granulite (C-833-A), showing a leucosome depleted in mafic minerals (mostly orthopyroxene and clinopyroxene); (B) peritectic orthopyroxene and clinopyroxene in a band of leucosome relatively enriched in mafic minerals (C-838-A); (C) Opdalite (C-838-2); and (D) enclave of mafic granulite with hornblende porphyroblasts (C-716-B). (For interpretation of the references to color in this figure legend, the reader is referred to the web version of this article.)

4.1.1. Petrographic interpretation

In the banded granulite C-833-A, the faint boundaries between melanocratic to mesocratic and leucocratic bands point to interactions between mafic and felsic components. The following compositional and textural features support this interpretation: i) the mafic minerals (orthopyroxene, clinopyroxene and hornblende) are the same in both melanocratic to mesocratic and leucocratic bands; ii) leucocratic phases of the mafic bands connect with those in the leucosomes (Fig. 4A). This suggests that they were formed, at least partially, by *in situ* partial melting.

4.2. Banded granulite (C-838-A)

Compared to sample C-833-A, the banded granulite C-838-A exhibits even fainter limits between bands of distinct composition (Figs. 4B and Fig. 5A). The dark green fine-grained band consists of hornblende (25–30 vol%) and oligoclase-andesine (45–50%), with nematogranoblastic texture. Orthopyroxene (< 5%) and traces of clinopyroxene are minor phases. Locally, the consumption of pyroxene by hornblende reveals a retrograde origin for the amphibole, which is overgrown by euhedral biotite (5 vol%) as the lowest temperature mineral. The light green charnockitic leucosome shows medium-grained granoblastic texture with sparse foliation traces. It comprises medium-grained anhedral orthopyroxene (10 vol%) and clinopyroxene (10–15%), weakly aligned along the banding, within a matrix composed of oligoclase (40–45%) and quartz (35–40%; Fig. 4B). Hornblende and biotite partially replace pyroxene grains. Quartz exhibits chessboard extinction. Plagioclase commonly shows anti-perthitic exsolutions. Apatite, zircon and ilmenite are accessory minerals in both mafic and felsic bands.

4.2.1. Mineral compositions

To investigate compositional variability at the micrometer scale, X-ray compositional maps were acquired by electron probe micro-analysis (EPMA) for the banded granulite C-838-A using 15 keV accelerating voltage, a specimen current of 100 nA and dwell times of 200 ms. The detailed analytical procedure is reported in Lanari et al. (2013, 2018). The semi-quantitative maps were standardized to maps of oxide weight percentage concentrations using internal standards (De Andrade et al., 2006) and the program XMAPTOOLS 2.3.1 (Lanari et al., 2014). Structural maps in atom per formula unit (a.p.f.u.) were used to investigate the local compositional variability of the mineral phases, as well as the mineral modes that were obtained from the phase map. The main compositional variations are related to the grain sizes and microstructural position of the mineral phases in the leucosome and mafic granulitic domains.

Orthopyroxene is mainly medium- to coarse-grained in the leucosome, and minor fine-grained in the mafic bands. In the leucosome, orthopyroxene exhibits slight compositional zoning from core to rim ($En_{56\text{-}48}Fs_{40\text{-}46}MgTs_{4\text{-}6}$; Fig. 5B, C and D). The image with the classified

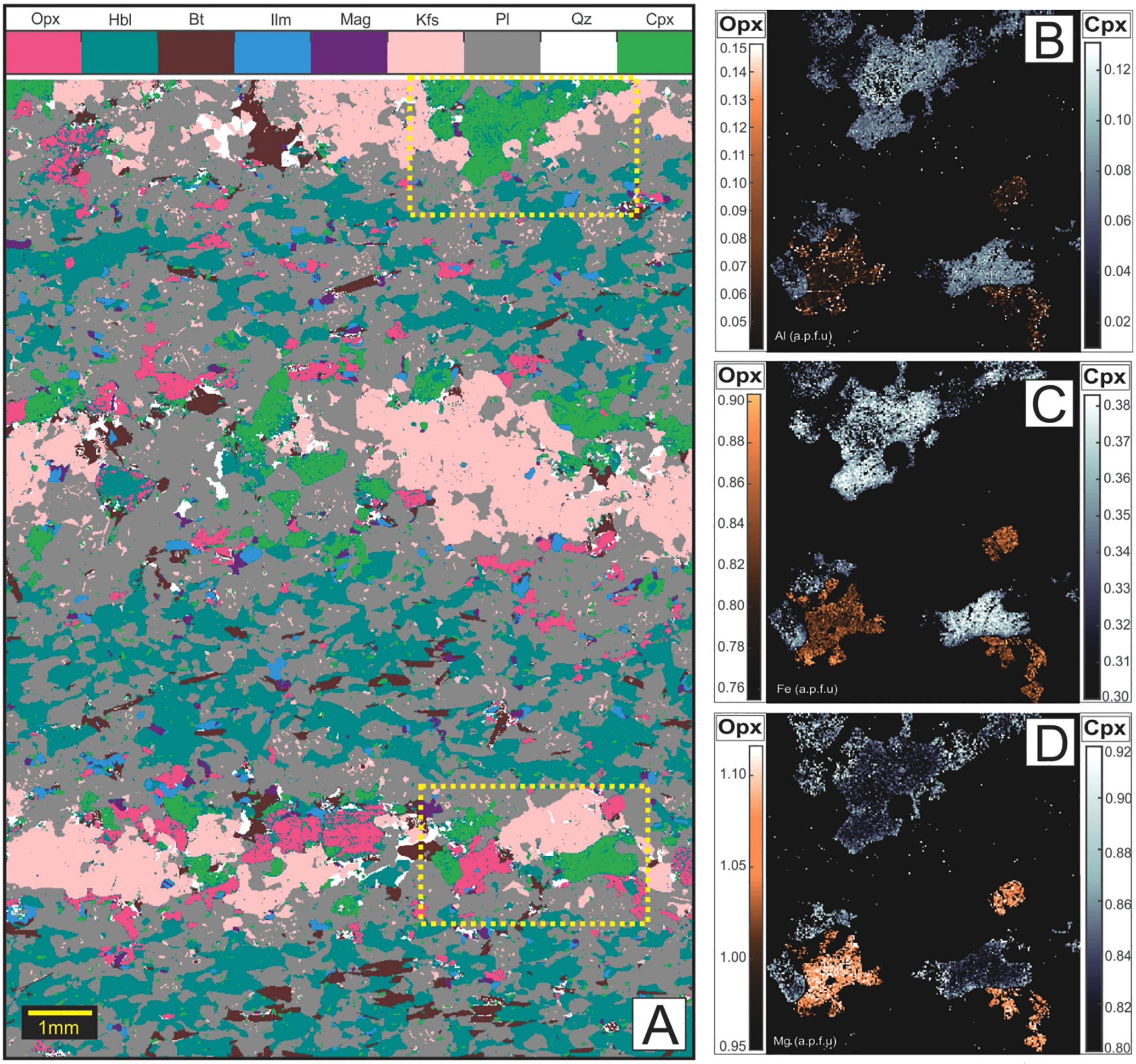

Fig. 5. Compositional maps from EPMA imaging: (A) Phase map showing the texture of the banded granulite (C-838-A) with assigned phases based on quantified compositional maps. Dotted yellow rectangles indicate the position of compositional maps for clinopyroxene and orthopyroxenes: (B) Al (a.p.f.u); (C) Fe (a.p.f.u); and (D) Mg (a.p.f.u). (For interpretation of the references to color in this figure legend, the reader is referred to the web version of this article.)

phases revealed that hornblende includes fine orthopyroxene grains in the mafic bands (Fig. 5A). These fine-grained inclusions display a similar variation ($En_{54-50}Fs_{41-43}MgTs_{5-7}$), but not forming a concentrically compositional zoning.

Optical microscopy shows medium-grained diopside in the leucosome (Fig. 4B). Sub-millimetric clinopyroxene occurs as rounded inclusions in large K-feldspar crystals (Fig. 5A). The compositional maps reveal fine-grained diopside inclusions in hornblende or plagioclase in the mafic bands. Occasionally, diopside and biotite inclusions are in contact one with each other (Fig. 5A). Diopside displays compositional zoning from core to rim in the leucosome ($Di_{60-70}Hd_{36-27}Jd_{5-4}$; Fig. 5B, C and D), and smaller compositional variations in the mafic bands ($Di_{63-65}Hd_{36-28}Jd_{6-4}$). Amphibole has a very homogeneous composition close to pure hornblende (Al in the site M2 = 0.6 a.p.f.u.; Na = 0.59 a.p.f.u.; Ca = 1.8 a.p.f.u.; and X_{Mg} = 0.11).

The phase map reveals that K-feldspar mainly forms clusters of coarse- to medium-grained crystals in the leucosome. K-feldspar also occurs as small inclusions in plagioclase and amphibole rims (Fig. 5A). At the contact with hornblende, K-feldspar porphyroblasts usually contain inclusions of fine-grained plagioclase and quartz, and rare clinopyroxene. K-feldspar crystals show compositional zoning from core ($Ab_{23}Mc_{77}$) to rim ($Ab_{10}Mc_{90}$).

Plagioclase texture and composition slightly vary from one band to another (Figs. 4 and 5): (i) in mafic bands, finer-grained plagioclase exhibits concentric zoning ($Ab_{68-65}An_{28-32}Mc_{3.5-3}$); (ii) in leucosome (felsic bands), plagioclase forms coarser-grained zoned crystals ($Ab_{70-66}An_{28-31}Mc_3$). The K fraction in plagioclase varies within the leucosome from K = 0.02 a.p.f.u., in the inner felsic band, to K = 0.04 a.p.f.u towards the mafic band.

Biotite composition also changes from one band to another. In the leucosome, biotite flakes have higher X_{Mg} (0.46–0.40 from core to rim) and lower Ti contents (0.23–0.20 a.p.f.u.), compared to lower X_{Mg} (0.36–0.42) and higher Ti contents (0.28–0.26 a.p.f.u.) in the mafic band.

4.2.2. Petrographic interpretation

Sample C-838-A, from a typical banded granulite composed of alternating mafic and felsic thin bands, shows evidence of physical interaction of the leucocratic phases from one band to another, both under optical microscopy (Fig. 4A) and EPMA imaging (Fig. 5A). The amount of K-feldspar and quartz is contrasting in the leucocratic bands, where K-feldspar clusters are typical features. Within the mafic bands, fine-grained K-feldspar and quartz have grown closely associated with plagioclase, hornblende and biotite (Fig. 5A), suggesting microfilms and pools of felsic melt (*cf*. Sawyer, 1999; Sawyer, 2008). In this scenario, the melt was preserved in the residue (*cf* Sawyer, 2008). The K-feldspar clusters suggest an *in source* partial melting process while the microfilms and pools suggest an *in situ* partial melting process responsible for the formation of the leucocratic (felsic leucosomes) and mesocratic to melanocratic bands (granulites or residues; Figs. 3F, 4B, 5A). Both residues and leucosomes show a granulitic mineral assemblages (Figs. 4B and 5A, Table 1).

4.3. Opdalite (C-838-2)

The light green, medium-grained rock (C-838-2) has opdalite composition, and displays foliated and isotropic domains, exhibiting equigranular texture (Fig. 4C). This sample consists of oligoclase (40–45 vol %), quartz (30–35%), orthoclase (8–10%), diopside-augite (5%) and orthopyroxene (5–8%; Fig. 4C). Orthopyroxene contains rounded plagioclase inclusions. Anhedral ilmenite is usually associated with pyroxene. Symplectite of biotite, ilmenite and quartz represents local disequilibrium features. Quartz often shows undulose extinction. Zircon, apatite and rutile are accessory phases.

4.4. Hornblende-biotite-bearing granitic leucosome (C-838-B)

The hornblende-biotite-bearing granitic leucosome C-838-B is a medium-grained leucocratic rock hosted by the stromatic metatexite (Fig. 3A). This leucosome is mainly composed of microcline, quartz and plagioclase, with modal contents varying from granite to granodiorite. The mafic minerals biotite (5 vol%), hornblende (3–5%) and actinolite (< 3%) display an incipient orientation. Perthite and antiperthite intergrowths are found in microcline and plagioclase, respectively. Myrmekite and block extinction are locally observed. Plagioclase is incipiently replaced by carbonate and sericite, and to a lesser extent by epidote and clinozoisite. Muscovite partly replaces biotite. Relicts of fine- to medium-grained schollen (Fig. 3E) have tonalitic composition containing hornblende (15 vol%) and biotite (10%). Together, ilmenite and pyrite constitute 5% of the mineral mode. Retrograde actinolite locally replaces hornblende. Rutile, zircon and apatite are accessory minerals.

4.5. Mafic granulite enclave (C-716-B)

The isotropic mafic granulite enclave (C-716-B) shows a dark green fine-grained matrix with scattered hornblende porphyroblasts (Fig. 4D). The granoblastic matrix consists of hornblende (55–60 vol%), plagioclase (15–20%), clinopyroxene (10–15%) and orthopyroxene (5–10%). Both pyroxenes show rounded inclusions of plagioclase and quartz. Retrograde hornblende porphyroblasts are up to 1 cm in size, they contain inclusions of all the matrix minerals. The amount of matrix inclusions increases towards the rim of the porphyroblasts. Quartz inclusions are much common, and retrograde biotite (3–5%) grew along hornblende fractures and borders. The accessory minerals are apatite, quartz and zircon. Opaque minerals (1%) are ilmenite, locally with magnetite exsolution, and minor pyrite and chalcopyrite.

5. Zircon U-Pb geochronology, Lu-Hf isotopes and *in situ* trace element microchemistry

Remarkable records of all the analyzed samples are protracted distributions of the zircon U-Pb spot data spreading along Concordia curves (Figs. 7 and 9). Therefore, a careful evaluation of the dates requires combination of distinct analytical approaches, linking chronometers and petrogenetic parameters. The main goals are to understand the meaning of these scattered data, and to unravel the ages of magmatic and metamorphic events. The term date (and related plural form) refer to individual time values from $^{206}Pb/^{238}U$ and $^{206}Pb/^{207}Pb$ spot data, while the term age is used for groups of $^{206}Pb/^{238}U$ and $^{206}Pb/^{207}Pb$ dates with geological significance. The analytical methods are described in Appendix A. In order to retrieve the protolith ages from high-grade metamorphic rocks, we used an approach similar to the one by Whitehouse and Kemp (2010), summarized below:

1) A detailed investigation of the internal structure of zircon through cathodoluminescence (CL) imaging to identify the core, successive rim generations, and single grains showing specific CL-responses, mostly neoformed (Fig. 6). Detailed descriptions of zircon populations from this study are reported in supplementary material S6.
2) U-Pb zircon core dates of one sample are assumed to represent a single magmatic event. The oldest grains in this data cluster are thus considered to represent the crystallization age while the younger dates are attributed to be the result of either Pb loss or resetting during metamorphism. These processes are especially relevant for rocks that were strongly affected by partial melting (Gerdes and Zeh, 2009; Rubatto, 2017; Vervoort and Kemp, 2016).
3) Lu-Hf analyses were carried out on zircon grains covering the respective date ranges and cathodoluminesce domains. The $^{176}Hf/^{177}Hf_{(t)}$ ratios were then used to reveal coupling or decoupling between the U-Pb and Lu-Hf systems (Gerdes and Zeh, 2009; Vervoort and Kemp, 2016; Wang et al., 2017; Whitehouse and Kemp, 2010). Hafnium signatures further provide hints towards possible melt sources and processes involved in the generation of the igneous protolith and the metamorphic products (Belousova et al., 2010; Dhuime et al., 2015; Taylor et al., 2016).

Additionally, in-situ trace element analyses on zircon were performed as these data can provide information to decode the protracted geochronological record in zircon, as well as be utilized for zircon thermometry (e.g., Kunz et al., 2018; Laurent et al., 2018). Trace element data are chondrite-normalized (McDonough and Sun, 1995). Titanium-in-zircon temperatures were calculated using the calibration of Watson et al. (2006). The opdalite (C-838-2) is the only sample containing the buffering assemblages, rutile + quartz for this system. In all other samples ilmenite is the stable Ti-phase, which means that the TiO_2 activity likely has been lower than 1 and that temperature estimates represent, at least, minimum values. For those samples, an average TiO_2 activity of 0.6 for metabasalts is assumed, following Ghent and Stout (1984). A detailed description of *in situ* REE abundance distributions and Ti-in-zircon thermometry is available in supplementary material S6.

The U–Pb, Lu-Hf and *in situ* trace element data of the analyzed zircon grains from samples C-833-A, C-838-2, C-838-A, C-838-B and C-716-B are presented in the supplementary materials S1, S2, S3, S4 and S5.

5.1. Banded granulite (C-833-A)

Cathodoluminescence (CL) images from zircon grains of the banded granulite reveal typical habits and textures of high-grade metamorphic zircons (Whitehouse and Kemp, 2010; Taylor et al., 2016), like subrounded grains, equant morphology, internal sector zoning textures with planar features of bright CL responses, and fir-tree zoning (sample 833-A; Fig. 6).

From 86 grains, 108 U-Pb spot analyses show spreading dates along the Concordia (Fig. 7A). Fifty-eight cores and entire grains with similar CL-responses with Th/U ratios between 0.1 and 1.3 outline a fairly

Fig. 6. Cathodoluminescence (CL) images of representative zircon grains. Location of the spot analyses: yellow circles for U-Pb dating with corresponding $^{206}Pb/^{238}U$ or $^{207}Pb/^{206}Pb$ dates (t) in Ma (spot size ~30 µm); blue dotted circles for trace elements (spot size ~20 µm); and dashed red circles for Lu-Hf ($\varepsilon Hf_{(t)}$; spot size ~50 µm). Samples: C-716-B, mafic granulite enclave; C-838-B, Hbl-Bt-bearing granitic leucosome; C-838-A, banded granulite; C-838-2, opdalite; C-833-A, banded granulite. (For interpretation of the references to color in this figure legend, the reader is referred to the web version of this article.)

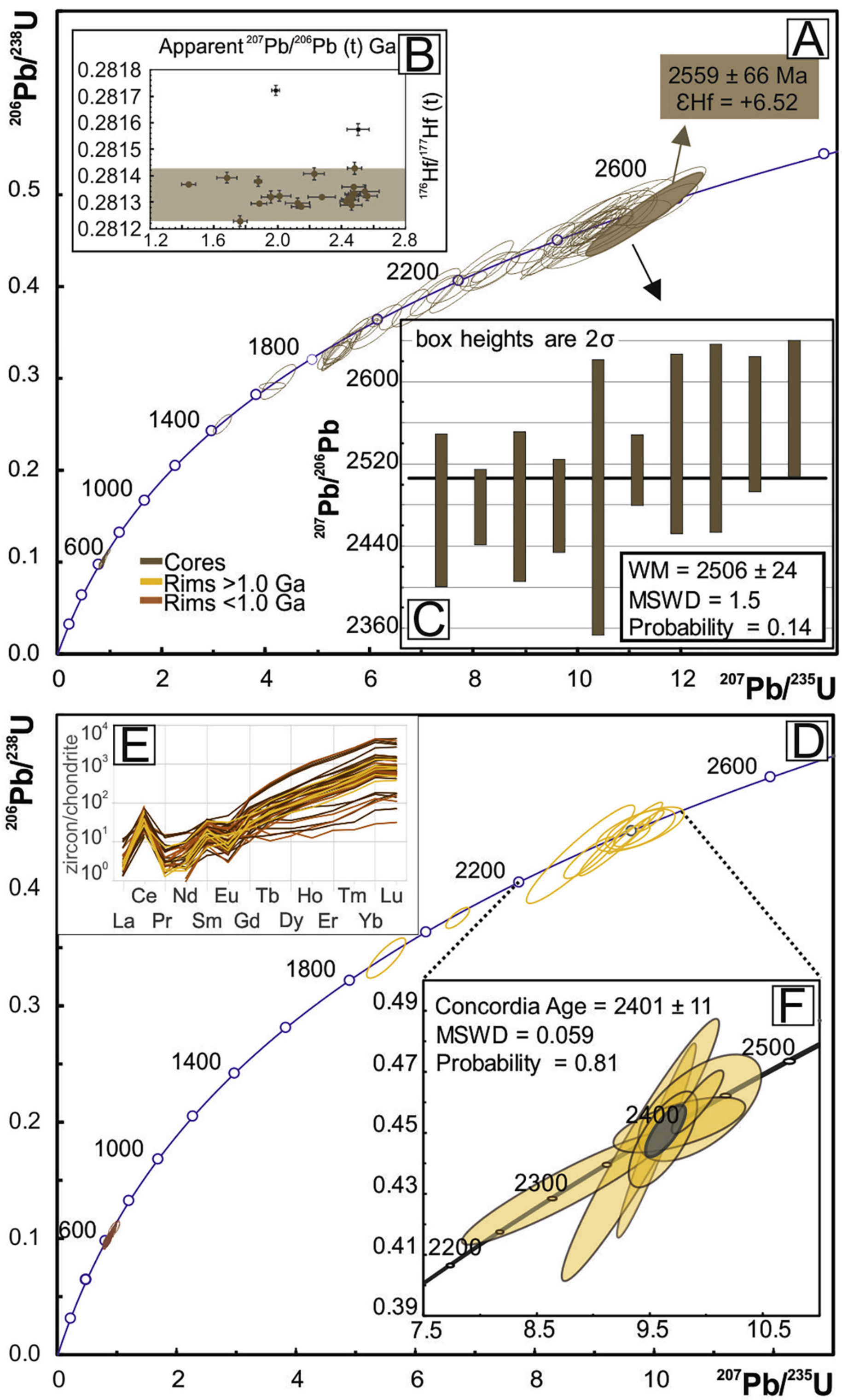

Fig. 7. U-Pb, Lu-Hf and trace elements zircon data for the banded granulite C-833-A. Data interpreted as magmatic (see text) are plotted in (A) Concordia diagram (ellipses: 2σ uncertainty); the brown filled ellipse represents the older grain containing $^{176}Hf/^{177}Hf_{(t)}$ within the cogenetic range from (B) initial $^{176}Hf/^{177}Hf_{(t)}$ ratio against age using $^{207}Pb/^{206}Pb$ dates; black squares correspond to possibly inherited grains; and (C) Weighted average age from the oldest 10 grains. (D) Concordia diagram (ellipses: 2σ uncertainty) for rims and single phases, (E) normalized zircon *vs* chondrite rare-earth elements diagrams for cores and rims; and (F) data that yielded a concordant age.

continuous spreading pattern in the Concordia from 2575 ± 66 Ma (the oldest $^{207}Pb/^{206}Pb$ date) to 1656 ± 82 Ma (Fig. 7A). Seven cores with $^{206}Pb/^{238}U$ dates cluster between 700 Ma and 600 Ma.

Eighteen grains from this sample were analyzed for Lu-Hf isotopes, resulting in $^{176}Hf/^{177}Hf_{(t)}$ ratios from 0.28123 to 0.28143, with only three of them exhibiting exceptional high $^{176}Hf/^{177}Hf_{(t)}$ values (0.28157–0.28172; Fig. 7B). The narrow $^{176}Hf/^{177}Hf_{(t)}$ range implies that zircon cores grew during a single magmatic event, constrained by their oldest dates around 2559 ± 66 Ma (Fig. 7A). To refine this estimate, a selection of the ten oldest grains provides a weighted average $^{206}Pb/^{207}Pb$ age of 2506 ± 24 Ma (MSWD = 1.5; Probability = 0.14; Fig. 7C). εHf recalculated for a crystallization age of 2550 Ma yields values between +10.0 and +2.72.

Rim and single-phase grain dates also spread along the Concordia (Fig. 7D). Their Th/U ratios range between 0.04 and 1.75 (n = 48). Most (80%) zircon rims yields clustered $^{206}Pb/^{238}U$ dates between 680 and 590 Ma (Fig. 7D). Data from almost exclusively bright CL rims provide the youngest date cluster (n = 17) with a concordant age of

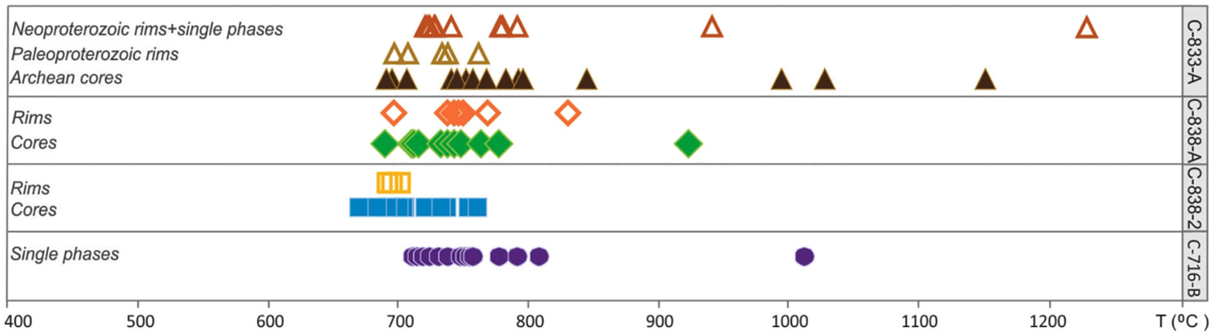

Fig. 8. Zircon crystallization temperatures from Ti-in-zircon thermometry using the calibration of Watson et al. (2006). Samples: C-833-A, banded granulite; C-838-A, banded granulite; C-838-2, opdalite; C-716-B, mafic granulite enclave.

607 ± 2 Ma. Lu-Hf analyses in six Neoproterozoic rims reveal $^{176}Hf/^{177}Hf_{(t)}$ between 0.28140 and 0.28187, and $\varepsilon Hf_{(t)}$ between −18.5 and −34.7.

The remaining 20% of zircon rims (n = 9) yield $^{207}Pb/^{206}Pb$ dates between 2425 ± 88 and 2351 ± 46 Ma, with two outliers at 1900 ± 52 and 2081 ± 32 Ma (Fig. 7F). The concordant age of 2405 ± 10 Ma (MSWD = 0.19; probability 0.67) is obtained from the six oldest grains. This range of metamorphic ages between 2.3 and 2.4 Ga, together with the lack of core dates between 2.3 Ga and 600 Ma, corroborate the interpretation of a metamorphic event around 2.4 Ga.

Trace element analyses of 49 zircon grains do not reveal differences in REE compositions between cores and rims of any age (Fig. 7E), as well as no undoubted correlation between the REE distribution and CL or age domains.

Titanium contents in zircon are variable. The group of Archean zircon cores exhibits Ti contents equivalent to temperatures of ~695–840 °C (average = 757 ± 45 °C; 1σ; n = 12). Three outliers yield temperatures of ca. 990 °C, 1025 °C and 1150 °C. The old rims (1680 and 2480 Ma) are relatively homogeneous in Ti with calculated temperatures of ~700–760 °C (average = 730 ± 26 °C; 1σ; n = 5). The Neoproterozoic rims have Ti contents corresponding to temperatures of ~720–790 °C (average = 727 ± 27 °C; 1σ; n = 9). Two rims yield temperatures of ~940 °C and ~1226 °C (Fig. 8).

5.2. Opdalite (C-838-2)

The zircon population comprises elongated bipyramidal grains with parallel oscillatory zoning, grains with irregular intermediate-CL responses (different shades of gray) and zircon exhibiting intermediate-CL responses lacking internal structures or with ghosts of older growth features. A number of zircon grains shows irregular-shaped, thin bright-CL rims less than 10 µm wide, locally reaching 30 µm, that usually overgrow older domains exhibiting lobate contacts (Fig. 6).

Eighty-one U-Pb spot analyses reveal a spreading set of concordant dates (Fig. 9). Cores and single grains with oscillatory zoning spread from ca. 790 Ma to ca. 620 Ma (Fig. 9A and C). The seven oldest grain dates range from 786 ± 10 Ma to 752 ± 5 Ma. The oldest date of 786 ± 10 Ma is interpreted as a minimum age for the magmatic protolith. Since rims are mostly absent or too thin for analysis, only six rim dates spread between ca. 690 Ma and 630 Ma (Fig. 6 and C). The absence of a date cluster prevents the distinction of a clear metamorphic age for this sample.

Lu-Hf analyses of twenty-nine grains, comprising the whole age spectrum, reveal very homogeneous signatures with $^{176}Hf/^{177}Hf_{(t)}$ from 0.28192 to 0.28199 (one grain reaches 0.28210), including two analyses of rims (Fig. 9B). $\varepsilon Hf_{(790)}$ ranges from −11.8 to −15.8 for the cores, and −12.6 to −13.4 for rims.

The zircon grains exhibit homogeneous REE patterns in the cores. Two analyses of the rare metamorphic grains and rims indicate slightly steeper REE slopes (Fig. 9D).

The opdalite shows Ti-in-zircon temperatures from 670 to 780 °C (average = 704 ± 29 °C; 1σ; n = 11) for the cores, and 690 to 700 °C (average = 694 ± 5 °C; 1σ; n = 3) for the rims (Fig. 8).

5.3. Banded granulite (C-838-A)

This rock usually shows bipyramidal, CL-dark, elongated to equant zircon grains. They show oscillatory to parallel zoning despite their subrounded habits. CL-bright unzoned rims, generally thinner than 20 µm, often overgrow zircon cores (Fig. 6).

Data from 101 U-Pb spot analyses on 96 zircon grains spread along the Concordia (Fig. 9). The $^{206}Pb/^{238}U$ dates range from ca. 690 Ma to ca. 595 Ma, for cores, and from ca. 670 to ca. 540 Ma, for the rims. The oldest grain has a $^{206}Pb/^{238}U$ date of 691 ± 3 Ma. The three oldest grains define a population with a weighted average $^{206}Pb/^{238}U$ age of 690 ± 3 Ma (MSWD = 0.41; Probability = 0.66).

To check a possible inheritance, the oldest and youngest grains of this population were analyzed for Lu-Hf, yielding $^{176}Hf/^{177}Hf_{(t)}$ around 0.28206–0.28207. Similar $^{176}Hf/^{177}Hf$ values were also obtained for other grains covering the full age spectrum for cores and single phases, displaying mostly homogeneous $^{176}Hf/^{177}Hf_{(t)}$ signals of 0.28199–0.28208 (Fig. 9F). Hence, the age of 691 ± 3 Ma can be interpreted as a minimum age of the magmatic protolith of the banded granulite.

Thirty-six rims and single grains with similar brightness in CL record a time span from ca. 670 to ca. 570 Ma. The dates define an asymmetric cluster from ca. 660 Ma to ca. 590 Ma, with a peak at 620–600 Ma in the probability density plot (Fig. 9G). Two rims are younger around 565 Ma (Fig. 9G).

Interestingly, the $^{176}Hf/^{177}Hf_{(t)}$ ratios (0.28199–0.28212) are similar for rims and cores (Fig. 9F). The $\varepsilon Hf_{(690)}$ values for the cores range from −8.2 to −12.6. One core of ca. 1333 Ma yields $\varepsilon Hf_{(t)}$ = +3.12. Rims have $\varepsilon Hf_{(t)}$ similar to the cores, ranging from −9.0 to −14.1.

The banded granulite C-838-A (n = 22) exhibits the highest variability of LREE in zircon contents among all samples. Cores, rims and neoformed zircon grains are somewhat similar in composition, with the neoformed grains exhibiting REE content range narrower than the cores (Fig. 9H).

Ti-in-zircon temperatures obtained for the cores are in the range of ~690–780 °C (average = 732 ± 26 °C; 1σ; n = 12), with one outlier of ~922 °C; and ~700–830 °C for the rims (average = 743 ± 40 °C; 1σ; n = 7; Fig. 8).

5.4. Hornblende-biotite-bearing granitic leucosome (C-838-B)

Heterogeneous morphology and CL-responses characterize this zircon population. There are short as well as minor elongated bipyramidal prismatic habits. Cathodoluminescence images disclose texturally heterogeneous grains, some of them exhibiting multiple rims

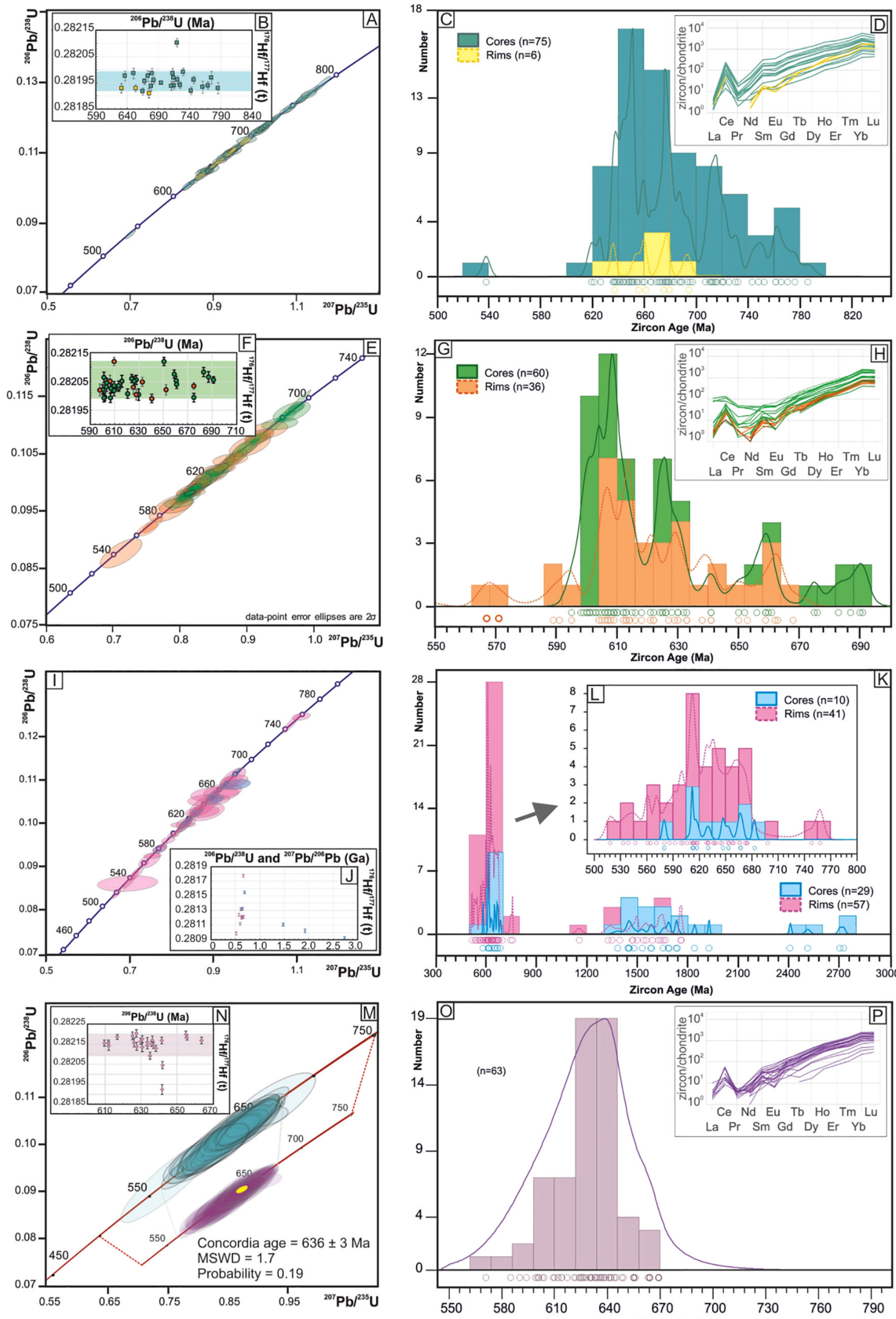

Fig. 9. Zircon data for Neoproterozoic rocks. U-Pb (Concordia and probability density diagrams), $^{176}Hf/^{177}Hf_{(t)}$ ratio *vs* age (using $^{206}Pb/^{238}U$ dates), and chondrite-normalized REE diagrams for: (A-D) opdalite C-838-2, cores in blue and rims in yellow; (E-H), banded granulite C-838-A, cores in green and rims in orange; (K-M) pink hornblende-biotite-bearing granitic leucosome C-838-B, cores in dark blue and rims in pink; (N-Q) mafic granulite enclave C-716-B. Ellipses in the Concordia diagrams are 2σ errors. (For interpretation of the references to color in this figure legend, the reader is referred to the web version of this article.)

(Fig. 6).

U-Pb data reveal a large range of concordant dates (Fig. 9I). Core dates scatter along the Concordia from ca. 2720 Ma to ca. 580 Ma, while rims spread from ca. 1761 Ma to ca. 520 Ma (Fig. 9K). A more detailed evaluation of each domain reveals that most core $^{207}Pb/^{206}Pb$ dates spread from ca. 2.7 Ga to 1.3 Ga, with Th/U ratios between 0.04 and 0.72 (n = 29). A subgroup of ten grains displays a date range of ca. 680 Ma to ca. 580 Ma (Fig. 9L). Such bimodal distribution is also observed for the rims (n = 57). Older rims cover an interval from ca. 1.7 Ga to ca. 1.4 Ga, while younger rims range between ca. 770 Ma and ca. 530 Ma.

Lu-Hf data for older cores of this sample display strong variability. $^{176}Hf/^{177}Hf_{(t)}$ ratios of the three oldest cores are 0.28093, 0.28102 and 0.28111, for $^{207}Pb/^{206}Pb$ dates of ca. 2725 Ma, ca. 1925 Ma and ca. 1479 Ma, respectively. Four younger cores yield $^{176}Hf/^{177}Hf_{(t)}$ ratios from 0.28120 to 0.28155, for $^{206}Pb/^{238}U$ ages between ca. 680 and ca. 580 Ma (Fig. 9J). Because $^{176}Hf/^{177}Hf_{(t)}$ ratios do not define a narrow compositional range, the protolith could have been either a sedimentary or an igneous rock.

Around 40% of the U-Pb analyses on cores provide dates in the range of ca. 680–580 Ma (Fig. 9L). These grains have CL-responses similar to the young rims, and $^{176}Hf/^{177}Hf_{(t)}$ ratios (0.28120–0.28155) distinct from the older group, suggesting they were much probably formed in the Late Neoproterozoic. Rims show highly crustal $\varepsilon Hf_{(t)}$ from -20.9 to -52.1, and $^{176}Hf/^{177}Hf_{(t)}$ between 0.28099 and 0.28177 (Fig. 9J). The rims data seem to be related to a main metamorphic event from ca. 600 to ca. 620 Ma.

5.5. *Mafic granulite enclave (C-716-B)*

Most grains show a sub-rounded morphology, sector zoning with CL-medium-bright responses, and faint but large oscillatory zoning (Fig. 6; Corfu et al., 2003). Some grains show fir-tree zonation and dark-CL responses from domains to the whole grain, and CL-brighter rims with grey hues around embayed cores (resembling zircon indentation). These rims are likely related to annealing (Corfu et al., 2003).

Sixty-three analyses on sector-zoned domains yield Th/U ratios between 0.35 and 2.02. Dates spread along the Concordia from ca. 670 to ca. 560 Ma (Fig. 9M). Most data (87%) define a Concordia age of 636 ± 2 Ma (Fig. 9M and O). However, $^{176}Hf/^{177}Hf_{(t)}$ form a narrow range between 0.28205 and 0.28220 (Fig. 9N), implying that the oldest grain (664 ± 9 Ma) can be interpreted as the crystallization age of a magmatic protolith. The $\varepsilon Hf_{(t)}$ values vary from -5.9 to -11.4 (n = 23). Grain # 5.1, presenting U-Pb date of 642 ± 8 Ma, is an outlier with $^{176}Hf/^{177}Hf_{(t)} = 0.28192$. This is the same value as recorded by the opdalite (C-838-2).

Zircon grains from the mafic granulite enclave have homogenous REE distribution patterns with the exception of Eu anomalies, which vary between slightly positive to highly negative values ($Eu/Eu^* = 0.12 – 1.12$; Fig. 9P). Titanium contents correspond to temperatures of ~710–810 °C with only one outlier showing $T = 1010$ °C (Fig. 8).

6. P-T estimates from mineral thermobarometry on the banded granulite (C-838-A)

In the banded granulite C-838-A, clinopyroxene and orthopyroxene are the mineral relicts of the peak metamorphic assemblage. Therefore, the orthopyroxene-clinopyroxene thermometer was applied to the compositional zones displayed by medium-grained orthopyroxene and clinopyroxene crystals (Fig. 5B–D). The calibration of Kretz (1982), based on the equilibrium exchange of Ca, Mg and Fe between clinopyroxene and orthopyroxene, yielded temperatures of 998 ± 23 °C (1 σ) for the cores and 916 ± 19 °C for the rims.

Retrograde conditions were estimated via amphibole crystallization from the equilibrium distribution of Na and Ca between plagioclase rims and hornblende, applying the edenite-tremolite calibration of Holland and Blundy (1994). Amphibole-plagioclase pairs yield a temperature of 740 ± 28 °C (1σ). Pressures were estimated on the same mineral pairs based on the Al content in amphibole (Hammarstrom and 1986; Hollister et al., 1987; Johnson and Rutherford, 1989). This method was previously applied by Del Lama et al. (2000) for similar rocks of the northern sector of the Guaxupé nappe. Calculated pressures range between 4 kbar and 7 kbar, with an average of 5.7 ± 0.9 kbar. The average *T* and *P* given here are reported together with a standard deviation value (1σ) obtained from the variability from the *P* and *T* maps (see Lanari et al., 2014, Lanari et al., 2018). This number reflects the relative uncertainties of the *P-T* estimates that are related to the analytical precision of the EPMA measurements (Lanari et al., 2013).

The Ti-in-biotite thermometer (Henry et al., 2005) yields temperatures that differ depending on the rock domain. The biotite flakes record slightly higher temperatures (750 ± 12 °C, 1σ) in the mafic bands than in leucosome ones (740 to 660 ± 57 °C).

7. Discussion

7.1. *Crystallization timing and petrogenesis of protoliths*

7.1.1. *U-Pb disturbed systems (all samples)*

Exceeding the analytical uncertainties, the spreading of U-Pb dates from zircon core along the Concordia is attributed to Pb loss with partial resetting during the UH*T* metamorphic event (see section 7.3; Figs. 7 and 9). The results suggest a partial decoupling of the U-Pb and Lu-Hf systems with preservation of the original Hf isotopic signatures (*cf* Vervoort and Kemp, 2016; Whitehouse and Kemp, 2010). This interpretation is further supported by inverse age zoning (i.e., younger cores than rims; Fig. 6; Laurent et al., 2018). In this context, U-Pb dates only support minimum crystallization ages because Pb could also have been lost prior to the thermal UH*T* metamorphic event. As εHf is age dependent, it can be underestimated for rocks that experienced Pb loss, especially for older rocks, as discussed by Vervoort and Kemp (2016).

Taking into account that zircon grains have experienced partial Pb loss, resulting in protracted age records (Figs. 7 and 9), previous interpretations suggesting inherited grains with ages around 800–700 Ma (e.g., Hackspacher et al., 2003; Rocha, 2016), may be questioned. Compared with the presented data, they would represent minimum crystallization ages. Furthermore, significant zircon inheritance is unlikely in mafic to intermediate magmas as zirconium solubility remarkably increases at high temperatures (Boehnke et al., 2013; Watson and Harrison, 1983).

7.1.2. *Neoarchean components*

Evidence of Neoarchean rocks involved in the Guaxupé nappe are preserved in the banded granulite (C-833-A) and hornblende-biotite-bearing granitic leucosomes (C-838-B).

Coupled U-Pb and Lu-Hf analyses of zircon indicate a minimum crystallization age of 2559 ± 65 Ma for the protolith of the banded granulite (C-833-A). Zircon cores have a juvenile signature with $\varepsilon Hf_{(2550)}$ between +10.0 and +2.72. The higher values are similar to εHf of depleted mantle (Fig. 10C; Blichert-Toft and Albarède, 1997). Most $\varepsilon Hf_{(2550)}$ signatures are mixtures between depleted mantle and the "new crust" that may have formed in intra-oceanic arc setting involving recycling of crustal material (Dhuime et al., 2011; Wang et al., 2017). Three zircon cores record crystallization temperatures higher than 900 °C for the mafic granulite C-833-A. Such high temperatures are in line with a basic composition of an igneous protolith (e.g., Grimes et al., 2009; Larsen, 1929).

An alternative interpretation, not favored here, may consider those ancient zircon grains as inheritance by contamination from an Archean crust. Against this, there is the great amount of grains older than 1.0 Ga found in the studied samples (i.e., > 60% of the analyzed grains), especially considering that no other rock records any Paleoproterozoic to Archean inheritance in the Guaxupé nappe. It is also unlikely that such amount of zircon would be preserved in a mafic rock that underwent to melting (e.g., Boehnke et al., 2013). A metasedimentary origin for the protolith of this mafic rock is clearly not supported by its steady $^{176}Hf/^{177}Hf_{(t)}$ signature, which indicates a very homogeneous juvenile source.

The isotopic signature of the melt source for the hornblende-biotite-bearing granitic leucosome (C-838-B) remains ambiguous. Three data points in the Hf evolution diagram, calculated from their respective individual $^{207}Pb/^{206}Pb$ dates (grains > 1 Ga), follow the average crustal evolution (Fig. 3.10A and C). Such signatures could indicate melts derived either from a sedimentary source or from heterogeneous igneous rocks that experienced Pb-loss with $\varepsilon Hf_{(2700)}$ between −4 and +4. In the first scenario of a sedimentary source, deposition could have happened at any time between the magmatic stage (2.7 Ga) and the onset of the Neoproterozoic metamorphism (ca. 680 Ma) owing to Pb loss at high temperatures (Fig. 9K). In the igneous hypothesis, the oldest grains record the magmatic crystallization age ($^{207}Pb/^{206}Pb$ = 2725 ± 19 Ma) and dates lower than 2725 Ma are the result of later disturbances. Cores yielding younger dates thereby likely record partial resetting during anatexis (Fig. 9L). Zircon inheritance preserving ages older than 1.0 Ga within a 680 Ma old rock that experienced partial melting to generate the C-838-B leucosome is improbable. Preservation of so many grains within a continuum spectrum distribution during two partial melting events, including an UH*T*-related metamorphism, appears highly unlikely. Thus, the only conclusion that can be drawn is that some 2.7 Ga-old crustal material contributed to form the hornblende-biotite-bearing granitic leucosome, instead of the juvenile 2.55 Ga basement.

7.1.3. Neoproterozoic rocks

Hosted by the Neoarchean basement, three different magmatic rocks have been identified based on their bulk rock compositions (Supplementary data S8), and U-Pb and Lu-Hf in zircon signatures (Fig. 10A and B), namely:

Opdalite C-838–2 – This rock records a magmatic event at 786 ± 10 Ma. The low $\varepsilon Hf_{(790)}$ values (−12.6 to −13.4) suggest a crustal origin for the magma. In the Hf evolution diagram (Fig. 10) the line of average crustal evolution is parallel to a line linking the Neoarchean juvenile basement (C-833-A) and the opdalite, indicating that the composition of the latter can result from partial melting of the former. A mixing with another source is suggested by the high $^{176}Hf/^{177}Hf_{(t)}$ of the opdalite. Anatexis of the lower crust was likely the main source of this opdalite. The crystallization temperatures between 670 and 780 °C are in line with this scenario.

Banded granulite C-838-A – The igneous zircon cores yield a magmatic crystallization age of 691 ± 3 Ma. The variable bulk rock compositions between the mafic and felsic bands (respectively from monzogabbro to granodiorite) could indicate magmatic differentiation of the original rocks, as well as residues and melts formed by anatexis. Like the opdalite, this sample exhibits a crustal $\varepsilon Hf_{(690)}$ signature (−8.2 to −12.6; Fig. 10C) that reflects partial melting of the basement. A mantle source possibly contributed to the formation of the basic rocks. The highest temperature of ~922 °C recorded in one igneous zircon core most likely represents the crystallization temperature, while temperatures of 690–780 °C recorded in all other cores are interpreted as underestimated crystallization temperatures due to lower TiO_2 activity. The latter could likewise record cooling temperatures. The banded granulites from basement (e.g., C-833-A) can only be distinguished from the Neoproterozoic rocks (e.g., C-838-A) through isotopic analyses.

Mafic granulite enclave C-716-B – The mafic granulite enclave is the youngest magmatic protolith found in the studied area, with a zircon crystallization age at 664 ± 9 Ma. It has a gabbroic composition and the least radiogenic Hf signature ($\varepsilon Hf_{(660)}$ = −5.9 to −11.4; Fig. 10C). The basic bulk rock composition and Hf signature indicate mixing between melt products from mantle and juvenile basement. The crustal Hf signature of the gabbroic enclave furthermore suggests that a metasomatic mantle source was involved. The younger crystallization age compared to the other protolith crystallization ages in the area points towards a later genesis compared to the mafic bands of the banded granulite. Ti-in-zircon thermometry provided temperatures between 710 and 810 °C, and up to 1010 °C for a single grain. Ti-in-zircon data usually record lower temperatures than major phases-based thermometers (Taylor et al., 2016), although similar temperatures have been reported for gabbroic magma crystallization as well as high Th/U in zircon (Grimes et al., 2009). Therefore, most calculated temperatures of 710–810 °C probably represent underestimates as the TiO_2 activity was likely < 1 (*cf* section 5).

The Neoproterozoic rock features and signatures are compatible with a volcanic-arc environment (supplementary data S7; Frost et al., 2001; Pearce et al., 1984). The εHf and lithochemical signatures in combination with the geochronological data, with the opdalite as oldest rock and the gabbronorite enclave as the youngest, indicate a progressively more juvenile Neoproterozoic magmatic activity in the Guaxupé nappe.

7.2. Petrochronological metamorphic evolution

The integration of the petrological evolution in a geochronological context permits a better understanding of the rock-forming processes, including the timing and the rates at which these processes occur (Engi et al., 2017). In the following section, *(P)-T* conditions are coupled with U-Pb ages, trace element and Lu-Hf in zircon signatures, in order to reconstruct the *(P)-T-t* path.

7.2.1. Conventional thermobarometric constraints

A robust determination of the peak conditions of the orthopyroxene-clinopyroxene granulites is not possible due to the lack of appropriate barometers. However, temperature estimates obtained for this unit can provide valuable insights when combined with *P* or *P-T* estimates available in the literature.

The cores of clinopyroxene and orthopyroxene are assumed to record the peak metamorphic conditions (T_{Peak}) with a temperature of 998 ± 23 °C (Table 1). Though pyroxene of mafic granulites could potentially resemble igneous relicts, two observations are in favor of an UH*T* metamorphic origin in addition to the recrystallized texture presented by orthopyroxene and clinopyroxene: (i) orthopyroxene-clinopyroxene thermometry yields temperatures compatible with peak *P-T* estimates obtained for a metasedimentary-derived orthopyroxene-garnet leucosome (1030 ± 110 °C and 11.7 ± 1.4 kbar; Rocha et al., 2017) and a garnet-bearing mafic granulite (ca. 1050 °C and 14 kbar; Del Lama et al., 2000); (ii) UH*T* metamorphism postdates (see section 7.3) the magmatic age of the protolith of the banded mafic granulite analyzed for thermometry (C-838-A) at ca. 690 Ma.

Post-peak temperatures (916 ± 19 °C) obtained from the pyroxenes rims (T_{R1}) are comparable with the peak conditions recorded in a garnet-bearing granulite (894 ± 4 °C and 11.9 ± 0.3 kbar; Rocha et al., 2018) and the post-peak conditions (865 ± 38 °C, 8.9 ± 0.8 kbar) obtained from garnet and orthopyroxene rims in orthopyroxene-garnet leucosome (Rocha et al., 2017).

A second retrograde stage (R2) corresponds to amphibole and plagioclase recrystallization at ~740 °C, as determined by amphibole-plagioclase thermometry. Biotite thermometry reveals similar temperatures of ~740 °C. Temperatures of R2 overlap within uncertainty with the retrograde temperatures of ~770 °C recorded by a garnet-bearing granulite (Rocha, 2016). Whereas *T* conditions are similar, the pressure estimates are different. Rocha et al. (2018) obtained *P* = 9 kbar for R1, in line with the results of Del Lama et al. (2000) for R2 on similar rocks. The pressure conditions obtained in this study are lower, around 6 kbar, despite using the same geobarometers as Del Lama et al. (2000). These differences could be related to different crustal levels that are now exposed within the nappe.

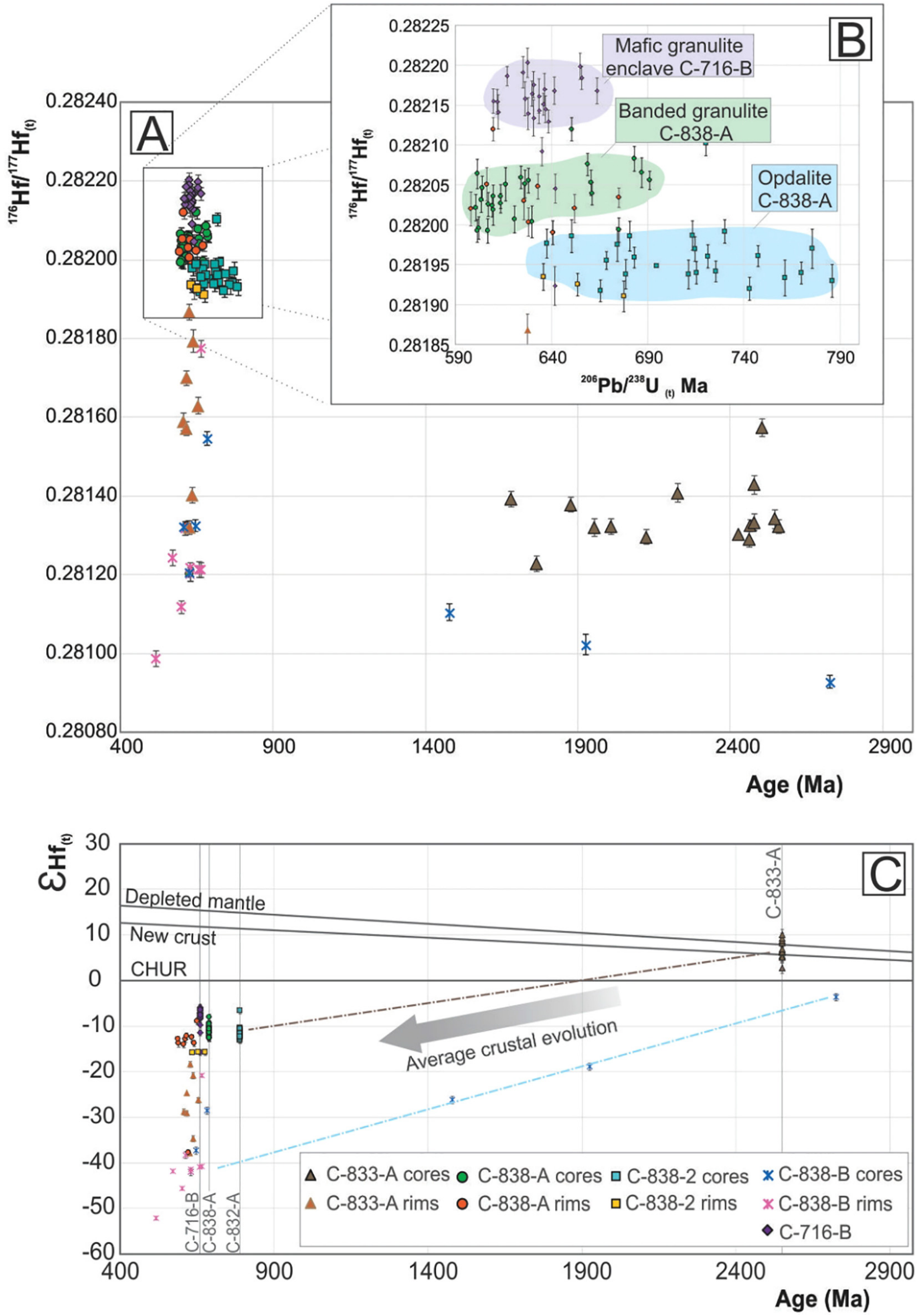

Fig. 10. Zircon Hf isotope data of the Guaxupé nappe rocks plotted as (A) initial $^{176}Hf/^{177}Hf_{(t)}$ ratio *vs* individual dates (*t*), using $^{207}Pb/^{206}Pb$ dates for grains older than 1 Ga and $^{206}Pb/^{238}U$ for younger grains, (B) Detail view of the Neoproterozoic rocks showing the Hf signature fields characteristic of each sample spreading along an approximately horizontal line and indicating different degrees of Pb loss, and (C) Hf-isotope evolution diagram with magmatic data being plotted as εHf recalculated for their crystallization ages (obtained from the oldest grain) and metamorphic data being plotted for their individual dates (*t*). Reference lines are: depleted mantle according to Blichert-Toft and Albarède (1997), chondrite of Griffin et al. (2000) and "New Crust" evolution line from Dhuime et al. (2011).

7.2.2. Temperature insights through zircon

High Th/U ratios of rims and neoformed zircon grains, especially for the samples showing Th/U up to 2, can be ascribed to high and ultra-high temperature rocks (Rubatto, 2002; 2017; Whitehouse and Kemp, 2010). Basic to intermediate compositions of the protoliths influence the Th supply, i.e., inhibiting monazite crystallization (Rubatto, 2017).

Only two zircon rims among the studied samples reveal ultrahigh temperatures by Ti-in-zircon thermometry. These data correspond to 655 Ma-old rims from the Neoarchean basement and record $T > 900$ °C (see Fig. 8). Despite the reduced number of grains recording UH*T* conditions, temperature results produced by contamination are unlikely, as no Ti-rich inclusions have been found in the zircon population (supplementary data S6). A possibly explanation is that these grains represent a minor population, formed by subsolidus crystallization (*cf* Rubatto, 2017). The Ti-in-zircon thermometer commonly yields lower temperatures than thermometers based on exchange equilibria (e.g. Ewing et al., 2013; Kohn et al., 2015). Such differences have been attributed to post-crystallization modification by diffusion or post peak crystallization (Baldwin et al., 2007; Korhonen et al., 2014; Taylor et al., 2016). For the studied rocks, most of the metamorphic zircon rims record retrograde temperatures of 700 °C that likely represent post-peak temperatures, since zircon records the cooling history rather than peak conditions in (ultra)-high grade rocks (Harley et al., 2007; Kohn et al., 2015).

7.2.3. Constraints of anatexis

Trace element bulk rock analyses of leucosomes exhibit positive Eu anomalies and depletions in HREEs, regardless of whether they are orthopyroxene-clinopyroxene-bearing or hornblende-biotite-bearing rocks. Such patterns are usual for feldspathic cumulates in leucosomes produced by low-degree partial melting (Sawyer, 1987). A similar petrogenesis can be constrained from REE in zircon (Figs. 7 and 9). In garnet-absent rocks, clinopyroxene is expected to have flat HREE patterns while orthopyroxene commonly fractionates, with accommodation and enrichment of the HREE compared to LREE (e.g., Yang and Wei, 2017). In the studied rocks, the REE patterns of zircon cores are retained in the younger rims. This indicates that there was no release or consumption of REE from other, e.g., mafic, phases that are the main HREE hosts. A limited interaction between melt and peritectic phases, e.g., due to a low degree of partial melting, is possibly the reason.

Distinct $^{176}Hf/^{177}Hf$ signatures are expected if zircon domains formed during different episodes of a rock evolution (Gerdes and Zeh, 2009; Rubatto, 2017). In the Guaxupé nappe, there are no differences between $^{176}Hf/^{177}Hf$ of zircon cores and rims of the Neoproterozoic banded granulite (C-838-A) and the opdalite (C-838-2) (Figs. 9 and 10). The preservation of primary $^{176}Hf/^{177}Hf$ compositions in metamorphic zircon is usually attributed to subsolidus recrystallization (Zeh et al., 2010). This can be explained by the absence of melting texture in the opdalite (C-838-2), in which there are fewer zircon rims with a smaller thickness (Figs. 6 and 11). In contrast, the preservation of similar $^{176}Hf/^{177}Hf$ ratios in zircon cores and rims of the banded granulite C-838-A, despite strong evidence for anatexis and interaction between melt and residue with crystallization of newly formed zircon grains, requires a distinct explanation. The key-indicators are: (i) diffuse contacts between leucosome and residue, (ii) films of melt along mineral boundaries in the residue, (iii) peritectic orthopyroxene and diopside in the leucosome, and (iv) quartz-feldspathic inclusions in zircon rims (Fig. 4B and 5A). The isotopic signatures rather suggest zircon crystallization from a small-volume melt, likely related to *in situ* melting (Taylor et al., 2016). Due to the presence of K-feldspar mainly in the leucosome bands, the melt can be also a result of *in source* melting (Fig. 5A). The fluid or melt that interacted with the growing zircon must have had a similar $^{176}Hf/^{177}Hf$ ratio, i.e., without significant contributions from the breakdown of Lu-host phases, such as of garnet or other ferromagnesian minerals (Melo et al., 2017; Taylor et al., 2016).

Another mechanism is required for the zircon rims of the banded granulite (C-833-A) and the pink hornblende-biotite-bearing granitic leucosome (C-838-B) that contain neoformed zircon grains with an increase of $^{176}Hf/^{177}Hf$ ratios compared to their protoliths, with the ratios exceeding the crustal evolution line trend. Such variation implies in an input of Hf with high $^{176}Hf/^{177}Hf$ ratios, which could also account for the difference of 20 εHf units between rims and cores, in the samples C-833-A and C-838-B. Zircon domains and grains with high $^{176}Hf/^{177}Hf_{(t)}$ compared to relict cores are generally interpreted to have crystallized in the presence of Hf-enriched melt and/or fluid (Chen et al., 2011). Release of radiogenic Hf into melts is thereby usually attributed to garnet breakdown (Zheng et al., 2005; Rubatto, 2017), apatite dissolution (Valley et al., 2010), or partial melting reactions involving breakdown of biotite (Melo et al., 2017). In the hornblende-biotite-bearing granitic leucosome (C-838-B) variable Hf ratios could be inherited, based on the assumption that the leucosome originated from melting of metasedimentary rocks (section 7.1.2). Since the source of the hornblende-biotite-bearing granitic leucosome C-838-B appears to include ancient crust (2.7 Ga), in contrast to its schollen diatexite host (ca. 690 Ma), such melt might have been allochthonous. Interactions between the hornblende-biotite-bearing granitic leucosome and orthopyroxene-clinopyroxene-bearing melts are suggested by field observations,

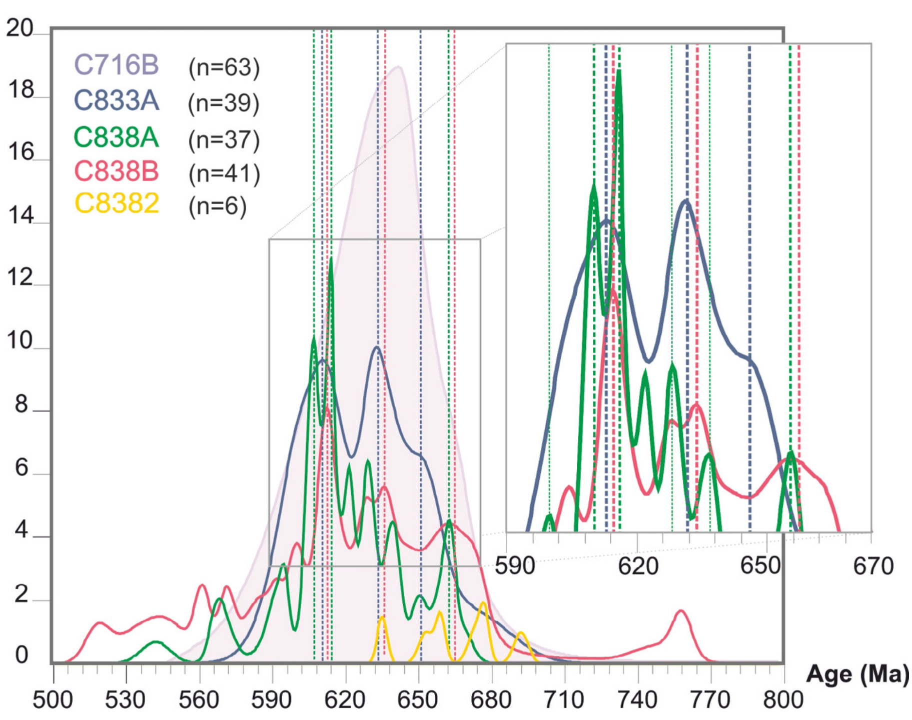

Fig. 11. Probability density diagram for the zircon U/Pb dates of the rims and single phases from the banded granulites (C-833-A and C-838-A), opdalite (C-838-2), and the hornblende-biotite-bearing granitic leucosome and the distribution of the dates from magmatic grains of the mafic granulite enclave (C-716-B) for comparison.

indicating melt mixing and further supporting an allochthonous melt origin (Figs. 3A and 4A). Melt-rock interactions are more likely to be the cause of the $^{176}Hf/^{177}Hf_{(t)}$ variability in sample C-833-A.

7.2.4. Age constraints and link to P-T conditions

Dating of zircon rims provides scattered $^{206}Pb/^{238}U$ dates showing complex distributions. Similar age probability peaks can be retrieved for different samples in an attempt to constrain the age of the successive metamorphic stages (Fig. 11). Zircon is particularly important as the orthopyroxene-clinopyroxene-bearing rocks do not contain any other geochronometer (such as monazite or titanite).

Growth, dissolution and re-precipitation of zircon can generally occur at any time during high temperature metamorphism and long periods of partial melting, thus explaining long-lasting metamorphic events registered by zircon ages (Laurent et al., 2018; Rubatto et al., 2013). Several processes such as metamictization, Pb-redistribution or diffusion can cause zircon resetting depending on the duration of the UH*T* stage (Harley, 2016). Multiple zircon ages (or dates) and cluster of ages (or dates) are further expected as a result of the evolution of (ultra) high-temperature terranes, because of dynamic zircon crystallization in the presence of melt. The resulting zircon compositional variability thereby commonly reflects zircon crystallization from segregated melts or interaction between different melts, with the respective zircon grains not necessarily exhibiting characteristic growth zones (Harley, 2016; Harley and Nandakumar, 2014). Thus, different domains are likely to record different ages. However, because analyses were performed on zircon separates, the influence of the domain in which the zircon is hosted cannot be retrieved.

The oldest metamorphic zircon dates suggest that the Neoproterozoic metamorphism started at ca. 680 Ma (Figs. 7, 8 and 11). The first but most discrete date peak is at ~660 Ma, recorded by zircon from the leucosomes from the banded granulites (C-833-A and C-838-A), and the pink hornblende-biotite-bearing granitic leucosome (C-838-B). Zircon data from the neoformed zircon grains and rims of the leucosome from the banded mafic granulite (C-833-A) define the next date peak at ca. 650 Ma. The three leucosomes show an intermediate peak around 640–630 Ma, succeeded by the most prominent date peak at 615–605 Ma, in the same samples. This stage corresponds to the most extensive zircon crystallization record. Zircon growth continued afterwards as indicated by a few zircon ages in the range of 590–550 Ma. Few dates younger than ca. 550 Ma are not statistically representative. The green charnockitic (C-838-A) and the hornblende-biotite-bearing granitic leucosomes share a common zircon growth history with a progressive increase of the crystallization rate of zircon around 615–600 Ma.

In summary, zircon age data suggest a long-lasting metamorphic event of at least 80 m.y. (670–590 Ma), including three main episodes of zircon growth at 670–650 Ma, 640–630 Ma, and 615–590 Ma.

The main arguments supporting coeval migmatization and emplacement of basic magma are: (i) the mafic enclave cannot be a residue because it has a younger age than the protolith of the host migmatitic rock; (ii) the basic magma emplacement age (ca. 660 Ma) is synchronous with the oldest peak of metamorphic zircon crystallization (Fig. 11); and (iii) two ca. 655 Ma zircon rims record $T > 900$ °C for the banded granulite (C-833-A). Therefore, it is much probable that a correlation exists between the ultrahigh temperatures recorded during the early metamorphic event and the emplacement of basic magma.

Zircon crystallization is strongly controlled by the composition and supply of melt (Rubatto, 2017; Rubatto et al., 2001), and is thought to proceed from late melts or along retrograde paths (Kohn et al., 2015; Tedeschi et al., 2017). Many younger zircon grains crystallized at ca. 630–600 Ma under temperatures between 690 and 830 °C. The large amount of zircon crystallization around 630–600 can be explained by widespread anatexis triggered by elevated temperatures during and after the UH*T* metamorphism, together with potential fluid input, during regional decompression.

The age of 630–625 Ma for the UH*T* peak conditions (~1030 °C at 12 kbar) was obtained by using EPMA monazite dating of resorbed Y-rich monazite cores preserved in garnet (Rocha et al., 2017). Those authors presented semi-quantitative maps and quantitative profiles on zoned garnet crystals, showing cores, that yield the peak conditions, enriched in Ca and Mg compared to the rims. The monazite grains exhibiting Y-rich cores, interpreted as prograde phases and attributed to pre-garnet growth (Rocha et al., 2017), are in the present contribution interpreted as inclusions in the boundaries between garnet Ca-rich cores and Ca-poorer rims, and most probably record retrograde conditions estimated ~860 °C and 9 kbar. Taylor et al. (2016) discussed that in some cases Y zoning in monazite may not reflect prograde conditions, resulting in misleading geological complex evolutions (e.g., Kelly et al., 2012; Spear and Pyle, 2010). That Y-enrichment could be explained by local dissolution of peritectic garnet during decompression or by the melt production associated with local Y supply. Because those monazites are Th-poor (Rocha et al., 2017), decompression before melting was more likely the driving process. A similar mechanism has been suggested for HREE-enrichments in zircon, which were related to garnet dissolution in H*P* amphibolites by Tedeschi et al. (2017). Yakymchuk (2017) considered that local variations in melt compositions around apatite could cause monazite crystallization. This process, known as pileup, is driven by slow diffusion and can generate heterogeneities in melt compositions (Harrison and Watson, 1984). The Y-rich domains around apatite with ages around 630 Ma, assigned to prograde decompression by Rocha et al. (2017), could thus represent the retrograde decompression in the Guaxupé nappe. The 630 Ma dates peaks from zircon (this study) and monazite (Rocha et al., 2017) can mark the onset of a retrograde *P-T-t* path (Figs. 11 and 12). We suggest that retrograde decompression between ca. 625 Ma and 600 Ma triggered widespread migmatization with overwhelming recrystallization of zircon (Figs. 11 and 12) together with Y-poor and Th-rich monazite (*cf* Rocha et al., 2017). In summary, the ultrahigh temperature metamorphism in the Guaxupé nappe would have started at ca. 660 Ma and was followed by a retrograde decompression metamorphic event with a peak of widespread migmatization and zircon crystallization at ca. 625–600 Ma.

7.3. UHT metamorphism in the Southern Brasília orogen

The tectonic settings in which ultrahigh temperature granulite metamorphism takes place are still intensely debated in literature (Harley, 2016; Kelsey and Hand, 2015 and references therein). According to Harley (2016), a key characteristic of granulite-UH*T* metamorphism in arc–back arc settings is the strong chronological link between magmatism, accretionary crustal growth and granulite development, as the accretion of juvenile crustal material can enhance conditions for granulite-UH*T* metamorphism. A key characteristic of arc-related settings for UH*T* metamorphism is the strong temporal link with major sedimentation, magmatism and metamorphism taking place within a short interval (5–20 m.y.).

An interval of ca. 30 m.y. marks the transition from "fast" to "slow" granulite-UH*T* metamorphism (Harley, 2016). The UH*T* metamorphism lasted for 40 m.y., at a maximum, in the Guaxupé nappe (see section 7.2.4). Some key features indicate that the studied UH*T* rocks were metamorphosed within a subduction-related magmatic arc system:

i) The magmatic protolith of a banded granulite (C-838-A) has a crystallization age of 691 ± 3 Ma, while the first neoformed zircon grains and rims yielded dates around 668 ± 7 Ma. This indicates a relatively short interval (ca.10–20 m.y.) between magmatic and metamorphic stages.
ii) There is an overlap between the metamorphic zircon ages of the leucosomes (section 7.2.3) and the magmatic ages of the mafic enclave (C-716-B), suggesting an input of mantle magma during a pre-collisional stage, inducing or increasing the metamorphic process.

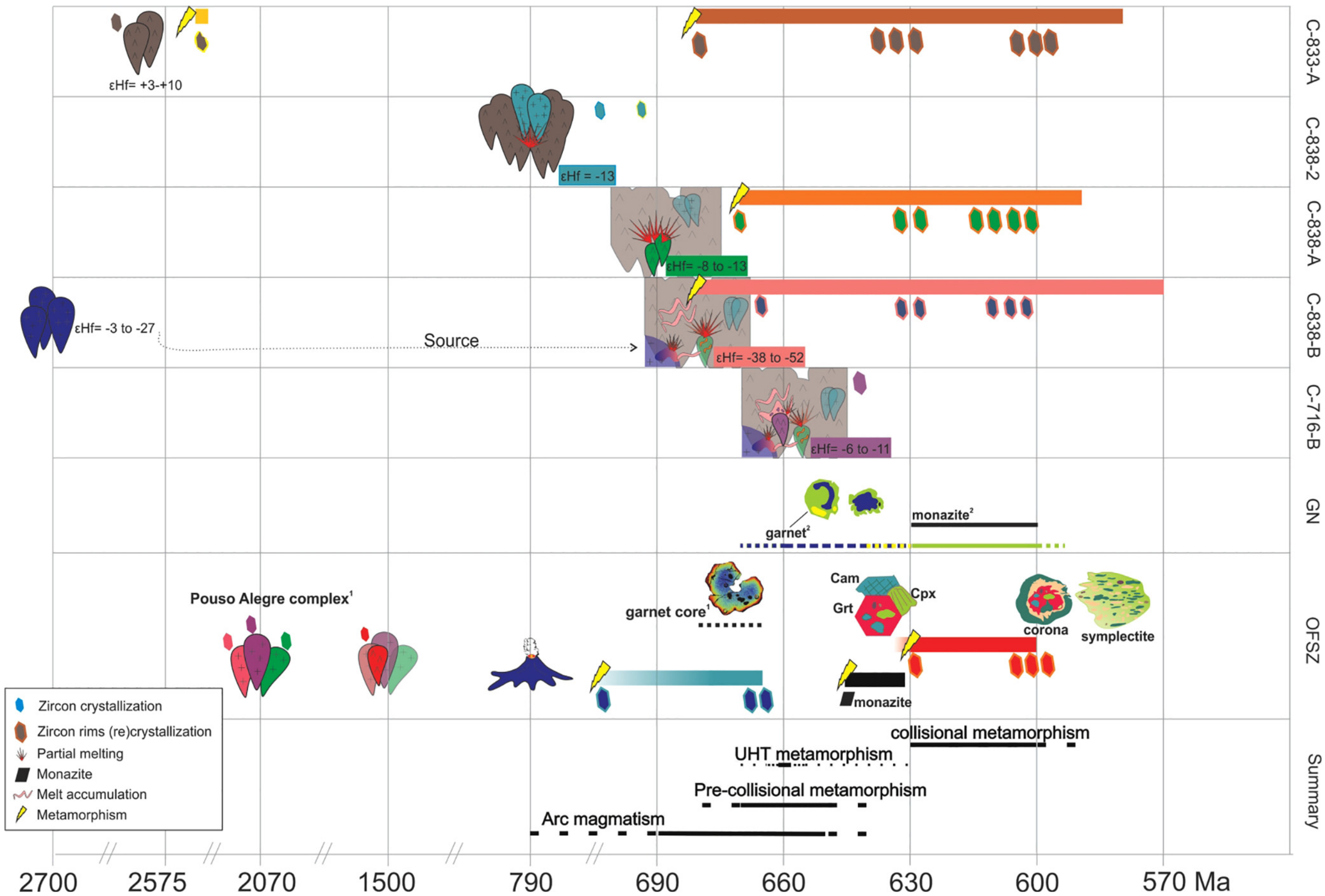

Fig. 12. Summary of the geological evolution of the Guaxupé nappe with emphasis on the temporal distribution, $\varepsilon Hf_{(t)}$ signatures and *P-T* constraints of igneous and metamorphic events of the studied samples. Data from (1) Tedeschi et al. (2017); (2 and 3) Rocha et al. (2017). Transparency applied to elements that constitute previous events, bright colors correspond to new events. Colors follow those used in the data presentation (Figs. 7–11). The distribution of zircon grains represented along the metamorphism bars indicate relative amount of zircon crystallization. GN –Guaxupé nappe; OFSZ – Ouro Fino Shear Zone.

iii) The two metamorphic zircon rims that yielded $T > 900\,^{\circ}C$ present $^{206}Pb/^{238}U$ dates at ca. 655 Ma. This is coeval with the emplacement age of the mafic enclaves.

iv) In the southernmost Brasília orogen, UH*T* conditions are restricted to the Guaxupé nappe. The metamorphic ages from 680 Ma to 630 Ma are likewise only recorded in the Guaxupé (this study) and Varginha nappes, the latter being placed directly below the former (*cf* Coelho et al., 2017). The Varginha nappe includes metasedimentary rocks ascribed to continental active margin (Campos Neto et al., 2011) or passive margin (Trouw et al., 2013).

A back-arc setting for the onset of UH*T* metamorphism is ruled out since high pressures (~12–10 kbar) are also recorded in the Guaxupé nappe. A thickened crust is more likely the cause for such high pressures and can also explain the crustal Hf isotopic signatures of the basic rocks. Indeed, crustal thickening by magmatic addition and intra-arc thrust tectonics is expected for long-lived arc systems on continental margins (Ducea, 2001; Thorpe et al., 1981). The crustal thickening could contribute with additional radioactive decay heat (Clark et al., 2011; Harley, 2016). Furthermore, the emplacement of basic magmas, represented by the mafic granulite enclave and *syn*-metamorphic mafic rocks in the nappe (e.g., Rocha et al., 2018), may have contributed to or induced ultrahigh to high temperature conditions as proposed in other regions (e.g., Ivrea Zone, Ewing et al., 2013; Val Malenco, Hermann et al., 1997). The basic magmas, however, unlikely were the only source of thermal energy as a much greater amount of magma than observed in the Guaxupé nappe would be necessary to induce such high temperatures (Ashwal et al., 1992). Thus, the ultrahigh temperature conditions more likely resulted from a combination of the aforementioned processes.

7.4. Regional implications for the southernmost Brasília orogeny

7.4.1. Disclosing the Paranapanema crust within the Guaxupé nappe

This paper presents the first evidence of Neoarchean juvenile basement involved in the Guaxupé nappe. The banded granulite (C-833-A) yielded the U-Pb zircon age of 2559 ± 65 Ma, with markedly positive $\varepsilon Hf_{(2550)}$ values (+10.0 to +2.72), thought to represent the crystallization of the magmatic protolith. The metamorphic age of 2401 ± 11 Ma is also a new finding for the Southern Brasília orogen. The age of ca. 2.4 Ga has as closest association with the earliest plutonic arc in the Mineiro belt in the São Francisco craton domain (Barbosa et al., 2018). Thus, data from the banded granulite (C-833-A) compared with the regional scenario, together with the allochthonous character of the area – part of the Guaxupé nappe – suggest that the ca. 2.55 Ga juvenile basement constitutes the first direct evidence of the Paranapanema block within the Guaxupé nappe. The allochthonous character likewise suggests that the zircon grains of ca. 2.7–1.5 Ga found in the hornblende-biotite leucosome also represents a contribution from the Paranapanema block.

Other basement rocks located close to, but outside the Guaxupé nappe are the Pouso Alegre (2.1 Ga; Cioffi et al., 2016a; Tedeschi et al., 2017), Amparo and Serra Negra complexes (3.0–2.7 Ga; Cioffi et al., 2016b), although their εHf signatures (+5.3 to +2.3) only overlap partially. This highlights the importance of juvenile to moderately juvenile components in the basement of the Southernmost Brasília orogen.

7.4.2. Neoproterozoic magmatism in the Guaxupé nappe

The first identification of an igneous rock of ~800 Ma (the opdalite C-838-2) brings new implications for the interpretation of terranes involved in the Guaxupé nappe. Igneous rocks of ca. 800 Ma have been described in the northern portion of the Brasília orogen for arc rocks with juvenile to slightly negative εNd (Pimentel and Fuck 1992; Pimentel, 2016). The youngest magmatic event in the Northern Brasília orogen took place between 670 and 630 Ma, presenting juvenile εNd signatures (Laux et al., 2005; Pimentel, 2016). In the Guaxupé nappe, however, crustal isotopic signatures are dominant.

The opdalite (C-838-2) may represent an early stage of arc magmatism, possibly related to the development of the Tonian arcs now located in the central and norther Brasília orogen. Zircon grains from ca. 800 Ma to ca. 730 Ma have been reported and interpreted as inheritance or xenocrystals in many rocks of the Guaxupé nappe. Such zircon grains may potentially reflect older protoliths than the ones previously invoked (e.g. Rocha, 2016; Vinagre et al., 2014 for the Socorro nappe). The εHf and lithochemical signatures point towards partial melting of a Neoarchean basement that acted as a significant source for the magmatic arc and/or contribution of a metasomatized mantle (Hagen-Peter et al., 2015; Rocha et al., 2018).

7.4.3. Evolution of the Guaxupé nappe

The geological evolution of the Guaxupé nappe can be divided into the following stages (Fig. 12):

(i) Onset of arc magmatism at ca. 790 Ma with the intrusion of magma of intermediate to felsic composition, mainly derived from lower crust with juvenile signature (Paranapanema block – $\varepsilon Hf_{(2550)}$ between +10.0 and +2.7).
(ii) Continuation or onset of intermediate to basic arc magmatism at ca. 690 Ma and beginning of arc-related metamorphism at ca. 680–670 Ma. This metamorphism is further registered in the metasedimentary rocks from the Varginha nappe, located below the Guaxupé nappe. Monazite dating in the Três-Pontas-Varginha nappe shows crystallization ages of 630–660 Ma (Reno et al., 2012) and zircon dating in the Ouro Fino Shear Zone, 672 ± 4 Ma (Tedeschi et al., 2017).
(iii) Intrusion of basic magmas having the most juvenile Hf signatures within the Neoproterozoic rocks. This magmatic activity, together with a long-lived arc-related magmatism and crustal thickening, triggered UH*T* metamorphism at ca. 660 Ma.
(iv) End of arc magmatism marked by the presence of mangerites emplaced at ca. 640 Ma with crustal $\varepsilon Hf_{(t)}$ (−5 to −10; Mora et al., 2014). This marks the transition from subduction to continental collision at ca. 640–630 Ma;
(v) Collision and decompression with extensive partial melting. This stage is marked by continuous monazite and zircon crystallization in the nappe from 630 to 600–590 Ma. The metamorphic peak conditions of the collisional stage recorded by the high-pressure amphibolite and migmatite of Pouso Alegre close to the nappe with 720 °C and 14 kbar at ca. 630 Ma. This stage was dated using zircon in the H*P* amphibolite, monazite in a sillimanite-garnet gneiss and zircon in the orthogneiss from the basement. A slow decompression of 1 mm.y^{-1} is recorded (Tedeschi et al., 2017).
(vi) Interference from the Ribeira orogeny (Trouw et al., 2013), orogen migration, or the onset of nappe faulting (Campos Neto et al., 2011) may have been partially recorded and can explain the ages younger than 600 Ma.

8. Conclusions

In this study, a new petrochronological dataset is presented for retrogressed UH*T* granulites of the Guaxupé nappe, Southern Brasília orogen. The main conclusions are:

- The basement of the Guaxupé nappe contains a juvenile ($\varepsilon Hf_{(2550)}$ = +2.7 to +10) Neoarchean (2559 ± 65 Ma), interpreted as a fragment from the Paranapanema block. It registers an old metamorphic stage at ca. 2.4 Ga, unlike other basement rocks of the Southern Brasília orogen.
- Coupled U-Pb and Lu-Hf in zircon analyses allow to the identification of Neoproterozoic magmatic rocks older than those so far found in the Guaxupé nappe. Such conclusions were previously only inferred from inherited zircon. The arc magmatism lasted at least from 690 to 640 Ma. The discovery of magmatic rocks of 786 ± 10 Ma indicates that magmatic activity started earlier within the terranes involved in the Guaxupé nappe. This can be correlated to other arcs located in the central and northern Brasília orogen.
- The Neoarchean juvenile basement acted as a source for the Neoproterozoic magmatism. A possibly metasomatized mantle source is also required, especially to form the gabbroic rocks.
- The nappe rocks experienced a long-lasting metamorphic event. From ca. 680 to ca. 640 Ma, related to arc development. Followed by a collision-to-decompression related metamorphism from ca. 640–630 to ca 600 Ma.
- Field evidence, petrography and $^{176}Hf/^{177}Hf_{(t)}$ ratios indicate that anatexis was driven by different processes, like: (i) incongruent *in situ* and *in source* partial melting without external melt contribution was the main anatexis process for the Neoproterozoic banded granulites and opdalites; and (ii) partial melting associated with inputs of allochthonous melt/fluid, possibly involving a crustal metasedimentary source, was dominant for the generation of hornblende-biotite-bearing granitic leucosomes.
- Peak temperatures of 998 ± 23 °C obtained in the mafic granulites can be linked to the arc-related UH*T* metamorphism.

The present study highlights the need for detailed investigations of other metamorphosed magmatic rocks in the Southern Brasília orogen. They could record similar disturbed U-Pb ages that can help to constrain the duration of UH*T* metamorphism and identify relicts of pre-UH*T* metamorphism.

Acknowledgments

This research was supported by the Brazilian “Science Without Borders Program” with a scholarship and grant to M. Tedeschi (Sandwich Dr stage in the University of Bern, CNPq 202054/2015-2), and by CODEMIG and CNPq projects coordinated by A. Pedrosa Soares. D. Rubatto and J. Hermann, University of Bern, are greatly thanked for fruitful discussions. C.E. Ganade and C. Valeriano thanked for discussion and suggestions. We also thank A. Alkmim, Universidade Federal de Ouro Preto, for analytical assistance with the LA-ICP-MS. The authors thank the comments and suggestions made by R. Moraes and R. Trouw, and the editorial handling by W. Teixeira and G. Zhao.

Appendix 3.A – Analytical methods

Sample preparation, imaging and qualitative analyses

Zircon was separated using standard rock crushing and heavy mineral separation techniques. Grains were individually selected, picked and mounted in epoxy resin. Grain months were polished to expose the grain centres. Zircons were imaged in cathodoluminescence (CL) for domain identification using a Quanta-250-FEI SEM fitted with a CL detector at the Multilab from Universidade do Estado do Rio de Janeiro (UERJ). For petrography, carbon-coated zircon mounts were investigated with a ZEISS EVO50 scanning electron microscope (SEM) at the Institute of Geological Sciences (University of Bern) with 20 keV acceleration voltage and beam current from 500 pA to 2000 nA at high vacuum conditions.

Bulk rock analysis

Major and trace element bulk rock compositions of four samples were analysed at the SGS GEOSOL laboratories (Brazil). Major element oxides were determined by XRF and trace elements by ICP-MS. Results are reported in Supplementary data S8.

Electron probe micro-analysis

The banded mafic granulite (C-838-A) was analysed by electron probe micro-analyser (EPMA) using both quantitative spot analyses and X-ray compositional mapping in wavelength-dispersive mode. EPMA analyses were carried out with a JEOL JXA-8200 superprobe at the Institute of Geological Sciences (University of Bern). Operating conditions for spot analyses were 15 keV accelerating voltage, 10 nA beam current and 40 s dwell times (including 2 × 10 s of background measurement). The following standards were used: wollastonite (Si), almandine (Fe), forsterite (Mg), orthoclase (K), anorthite (Ca), albite (Na) and ilmenite (Ti). Compositional maps were acquired following the procedure described in Lanari et al. (2012; 2013) using 15 KeV accelerating voltage, 100 nA beam current and dwell times of 200 ms. A map of 700,000 pixels over an area of 700 × 1000 μm^2 with a spot size of 20 µm × 20 µm was acquired. Spot measurements were also carried out in the same area to be used as internal standards (De Andrade et al., 2006). Results are presented in Supplementary data S3.

The compositional maps were classified and converted into concentration maps of oxide weight percentage using the software XMAPTOOLS 2.3.1 (Lanari et al., 2014).

Trace elements LA-ICP-MS

Trace elements compositions were obtained using a Thermo-Scientific Finnigan Element 2 SF-ICP-MS coupled to a CETAC213 ultraviolet laser system at the Isotope Geochemistry Laboratory of the Universidade Federal de Ouro Preto, Brazil. Conditions for laser fluency, frequency and spot size were 3 J/cm^2, 6 Hz and 20 µm. Both the acquisition and reduction data were performed in blocks of 120 analyses using NIST SRM 612 as primary standard and NIST SRM 610, USGS BCR-1 and USGS BHVO-2G as secondary reference materials. The software Glitter (van Achterbergh et al., 2001) was used for processing the time-resolved signal data. The internal standard value for zircon was SiO_2 = 32.78 wt%. Spots were placed near or comprising one third of the position of the U-Pb dating spots and in the same CL-domains. The results are also within error of recommended values. The results from trace elements in zircon analyses are available in the Supplementary data S1 for C-833-A, S2 for C-838-2, S3 for C-838-A, S4 for C-838-B and S5 C-716-B.

LA-ICP-MS U-Pb zircon dating

U-Pb isotopic analyses were performed with two LA-ICP-MS systems: (1) Samples C-838-A, C-838-2 and C-838-B were analysed with a Thermo-Finnigan Neptune multicollector ICP-MS (Thermo-Finnigan Neptune multicollector) coupled to a Photon-Machines 193 nm G2 laser system at Universidade Federal de Ouro Preto (UFOP) following the procedure described in Santos et al. (2017). Instrument set up parameters were a spot size of 20 µm, a frequency of 6 Hz, 10% energy with an intensity of 0.3 mJ. U-Pb data were standardized using the zircon GJ-1 (reference 609 Ma, Jackson et al., 2004) as primary standard and tested using the zircon Pleisovice (reference 337 Ma, Slama et al., 2008) as secondary standard. External errors were propagated considering the internal reproducibility of the individual ratios, external reproducibility of GJ-1, long-term uncertainty of the validation material, ratio uncertainties of the reference material and Pb-common ratio uncertainty (Lana et al., 2017). (2) Samples C-833-A and C-716-B were analysed with the microprobe ArF Excimer Laser 193 µm da Photon (Machines Inc. Model ATLEX SI) coupled to the high-resolution Neptune-Plus multicollector (Thermo Fisher Scientific, USA), at the MULTILAB, Universidade do Estado do Rio de Janeiro (UERJ). Instrument set up parameters were 6–7 mJ/cm^2 laser fluency, 10 Hz, 25 µm and Laser energy spot between 60 and 70%. U-Pb data were standardized using GJ-1 zircon (reference 609 Ma, Jackson et al., 2004) as primary standard and tested using the zircon 91,500 (reference 1065 Ma, Wiedenbeck et al., 1995) as secondary standard. External errors were calculated with the error propagation of individual measurements of GJ-1 and the individual measurements of each spot. Data reduction was done using an Excel program developed by Chemale et al. (2012).

Data evaluation for each spot was filtered considering outliers values of common Pb contents, errors of isotopic ratios and high percentages of discordance and Th/U ratios. The Concordia diagrams were obtained using the software Isoplot/Ex (Ludwig, 2003) and the histograms and probability density plots with Density Plotter (Vermeesch, 2012). Individual uncertainties are presented at 2σ level. The confidence level for the weighted averages is 95%. The results from U-Pb LA-ICP-MS analyses are available in the Supplementary data S1–S5 for C-833-A, C-838-2, C-838-A, C-838-B and C-716-B.

Lu-Hf in zircon analyses

Data were obtained using a Thermo-Finnigan Neptune multicollector ICP-MS coupled to a Photon-Machines 193 nm laser system (LA-MC-ICP-MS, Photon machines 193/Neptune Thermo Scientific), at Universidade Federal de Ouro Preto, Brazil. Data were collected as described in Santos et al. (2017). Spots were placed near or comprising partially the position of the U-Pb dating spots or in the same CL-domains. The laser was operated with a spot of 50 µm in diameter (60% power), fluence of 4.54 J/cm, and a pulse rate of 6 Hz. Both the acquisition and reduction data were performed in blocks of 160 analyses interspersed with the following reference materials: BB ($^{176}Hf/^{177}Hf$ = 0.281674 ± 0.000018; Santos et al., 2017), GJ1 ($^{176}Hf/^{177}Hf$ = 0.282000 ± 0.000005; Morel et al., 2008) and Plešovice ($^{176}Hf/^{177}Hf$ = 0.282481 ± 0.000014; Slama et al., 2008). The results are also within error of recommended values. The results from Lu-Hf LA-ICP-MS analyses are available in the Supplementary data S1–S5 for samples C-833-A, C-838-2, C-838-A, C-838-B and C-716-B.

Appendix A. Supplementary data

Supplementary data associated with this article can be found, in the online version, at https://doi.org/10.1016/j.precamres.2018.07.023.

References

Ashwal, L.D., Morgan, P., Hoisch, T.D., 1992. Tectonics and heat sources for granulite metamorphism of supracrustal-bearing terranes. Precambr. Res. 55, 525–538.

Baldwin, J.A., Powell, R., Brown, M., Moraes, R., Fuck, R.A., 2005. Modelling of mineral equilibria in ultrahigh-temperature metamorphic rocks from the Anápolis-Itauçu Complex, central Brazil. J. Metamorph. Geol. 23 (7), 511–531.

Baldwin, J.A., Brown, M., Schmitz, M.D., 2007. First application of titanium-in-zircon thermometry to ultra-high temperature metamorphism. Geology 35, 295–298.

Barbosa, N., Teixeira, W., Ávila, C.A., Montecinos, P.M., Bongiolo, E.M., Vasconcelos, F.F., 2018. U-Pb geochronology and coupled Hf-Nd-Sr isotopic-chemical constraints of the Cassiterita Orthogneiss (2.47-2.41 Ga) in the Mineiro belt, São Francisco craton: Geodynamic fingerprints beyond the Archean-Paleoproterozoic Transition. Precambrian Res. https://doi.org/10.1016/j.precamres.2018.01.017.

Bègin, N.J., Pattison, D.R.M., 1994. Metamorphic evolution of granulites in the Minto Block, northern Québec: extraction of peak P-T conditions taking account of late Fe-Mg exchange. J. Metamorph. Geol. 12, 411–428.

Belousova, E., Griffin, W., O'Reilly, S.Y., Fisher, N., 2002. Igneous zircon: trace element composition as an indicator of source rock type. Contrib. Miner. Petrol. 143, 602–622.

Belousova, E.A.Y.A., Kostitsyn, W.L., Griffin, G.C., BeggO'Reilly, S.Y., Pearson, N.J., 2010. The growth of the continental crust: constraints from zircon Hf-isotope data. Lithos 119, 457–466.

Blichert-Toft, J., Albarède, F., 1997. The Lu-Hf geochemistry of chondrites and the evolution of the mantle-crust system. Earth Planet. Sci. Lett. 148, 243–258.

Boehnke, P., Watson, E.B.B., Trail, D., Harrison, T.M.M., Schmitt, A.K.K., 2013. Zircon

Saturation Re-Revisited. Chem. Geol. 351, 324–334.
Brito Neves, B.B., Campos Neto, M.C., Fuck, R.A., 1999. From Rodinia to Western Gondwana: an approach to the Brasiliano-Pan African cycle and orogenic collage. Episodes 22, 155–166.
Campos Neto, M.C., Basei, M.A.S., Vlach, S.R.F., Caby, R., Szabó, G.A.J., Vasconcelos, P., 2004. Migração de orógenos e superposição de orogêneses: um esboço da colagem Brasiliana no sul do Cráton do São Francisco, SE e Brasil. Geologia USP Série Científica 4 (1), 13–40.
Campos Neto, M.C., Basei, M.A.S., Janasi, V., Moraes, R., 2011. Orogen migration and tectonic setting of the Andrelândia Nappe system: an Ediacaran western Gondwana collage, south of São Francisco craton. J. S. Am. Earth Sci. 32, 393–406.
Campos Neto, M.C., Caby, R., 1999. Neoproterozoic high-pressure metamorphism and tectonic constraint from the nappe system south of the Sao Francisco Craton, southeast Brazil. Precambr. Res. 97 (1–2), 3–26.
Campos Neto, M.C., Caby, R., 2000. Lower crust extrusion and terrane accretion inthe Neoproterozoic nappes of southeast Brazil. Tectonics 19, 669–687.
Campos Neto, M.C., Figueiredo, M.C.H., 1995. The Rio Doce orogeny, southeastern Brazil. J. South Am. Earth Sci. 8 (2), 143–162.
Carrington, D.P., Harley, S.L., 1995. Partial melting and phase relations in high-grade metapelites: an experimental petrogenetic grid in the KFMASH system. Contrib. Miner. Petrol. 120, 270–291.
Chemale, F., Kawashita, K., Dussin, I.A., Avila, J.N., Justino, D., Bertotti, A., 2012. U-Pb zircon in situ dating with LA-MC-ICP-MS using a mixed detector configuration. Anais da Academia Brasileira de Ciências 84, 275–295.
Chen, Y.-X., Zheng, Y.-F., Chen, R.-X., Zhang, S.-B., Li, Q., Dai, M., Chen, L., 2011. Metamorphic growth and recrystallization of zircons in extremely ^{18}O-depleted rocks during eclogite-facies metamorphism: Evidence from U-Pb ages, trace elements, and O–Hf isotopes. Geochim. Cosmochim. Acta 75, 4877–4898.
Cherniak, D.J., 2010. Diffusion in accessory minerals: zircon, titanite, apatite, monazite and xenotime. Rev. Mineral. Geochem. 72, 827–869. https://doi.org/10.2138/rmg.2010.72.18.
Cherniak, D.J., Watson, B.E., 2003. Diffusion in zircon. Rev. Mineral. Geochem. 53, 113–143.
Cioffi, C.R., Campos Neto, M.C., Möller, A., Rocha, B.C., 2016a. Paleoproterozoic continental crust generation events at 2.15 and 2.08 Ga in the basement of the southern Brasília Orogen, SE Brazil. Precambrian Res. 275, 176–196.
Cioffi, C.R., Campos Neto, M.C., Möller, A., Rocha, B.C., 2016b. Tectonic significance of the Meso- to Neoarchean complexes in the basement of the southern Brasília Orogen. Precambr. Res. 287, 91–107.
Clark, C., Fitzsimons, L.C.W., Healy, D., Harley, S.L., 2011. How does the continental crust get really hot? Elements 7, 235–240.
Coelho, M.B., Trouw, R.A.J., Ganade, C.E., Vinagre, R., Mendes, J.C., Sato, K., 2017. Constraining timing and P-T conditions of continental collision and late overprinting in the Southern Brasília Orogen (SE-Brazil): U-Pb zircon ages and geothermobarometry of the Andrelândia Nappe System. Precambr. Res. 292, 194–215.
Cordani, U.G., Brito-Neves, B.B., D'Agrella-Filho, M.S., 2003. From Rodinia to Gondwana: a review of the Available Evidence from South America. Gondwana Res. 6 (2), 275–283.
Cordani, U.G., Brito Neves, B.B. de B., Fuck, R.A., Thomaz Filho, A., Cunha, F. M. B., 1984, Estudo preliminar de integração do Pré-Cambriano com os eventos tectônicos da Bacias Sedimentares Brasileiras. Revista Ciência-Técnica-Petróleo. Secção Exploração de Petróleo. Petrobrás/Cenpes/Sintep, 15, p. 70.
Cordani, U.G., Nutman, A.P., Coutinho, J.M.V., 2002. Geochronological constraints on the evolution of the Embu complex. J. S. Am. Earth Sci. 14, 903–910.
Corfu, F., Hanchar, J.M., Hoskin, P.W.O., Kinny, P., 2003. Atlas of zircon textures. In: Hanchar, J.M., Hoskin, P.W.O. (Eds.), Zircon. Reviews in Mineralogy and Geochemistry, pp. 469–500.
De Andrade, V., Vidal, O., Lewin, E., O'Brien, P., Agard, P., 2006. Quantification of electron microprobe compositional maps of rock thin sections: an optimized method and examples. J. Metamorph. Geol. 24, 655–668.
Degler, R., Zogheib, F.F., Martins, L.C.D., Novo, T., 2015. Geologia das Folha Nova Resende (SF.23-V-D-I) 1:100.000. Projeto Fronteiras de Minas, CODEMIG-UFMG, Belo Horizonte, Brazil.
Del Lama, E.A., Zanardo, A., Oliveira, M.A.F., Morales, N., 2000. Exhumation of high pressure granulites of the Guaxupé complex, southeastern Brazil. Geol. J. 35, 231–249.
Dhuime, B., Hawkesworth, C., Cawood, P., 2011. When continents formed. Science 331, 154–155.
Dhuime, B., Wuestefeld, A., Hawkesworth, C.J., 2015. Emergence of modern continental crust about 3 billion years ago. Nat. Geosci. 8, 552–555.
Drüppel, K., Elsäßer, L., Brandt, S., Gerdes, A., 2013. Sveconorwegian mid-crustal ultrahigh-temperature metamorphism in Rogaland, Norway: U-Pb LA-ICP-MS geochronology and pseudosections of sapphirine granulites and associated paragneisses. J. Petrol. 54, 305–350.
Ducea, M., 2001. The California arc: Thick granitic batholiths, eclogitic residues, lithospheric-scale thrusting, and magmatic flare-ups. GSA Today 11 (11), 4–10.
Engi, M., 2017. Petrochronology based on REE–minerals: monazite, allanite, xenotime, apatite. In: Kohn, M.J., Engi, M., Lanari, P. (Eds.), Petrochronology. Reviews in Mineralogy and Geochemistry, pp. 365–418.
Engi, M., Lanari, P., Kohn, M., 2017. Significant Ages – An Introduction to Petrochronology. In: Kohn, M.J., Engi, M., Lanari, P. (Eds.), Petrochronology. Reviews in Mineralogy and Geochemistry 83, pp. 55–102.
Ewing, T., Hermann, J., Rubatto, D., 2013. The robustness of the Zr-in-rutile and Ti-in-zircon thermometers during high-temperature metamorphism (Ivrea-Verbano Zone, northern Italy). Contrib. Miner. Petrol. 165, 757–779.
Frost, B.R., Barnes, C.G., Collins, W.J., Arculus, R.J., Ellis, D.J., Frost, C.D., 2001. A geochemical classification for granitic rocks. J. Petrol. 42, 2033–2048.
Gerdes, A., Zeh, A., 2009. Zircon formation versus zircon alteration-New insights from combined U-Pb and Lu–Hf in-situ LA-ICP-MS analyses, and consequences for the interpretation of Archean zircon from the Central Zone of the Limpopo Belt. Chem. Geol. 261, 230–243.
Ghent, E.D., Stout, M.Z., 1984. TiO2 activity in metamorphosed pelitic and basic rocks-principles and applications to metamorphism in southeastern Canadian cordillera. Contrib. Miner. Petrol. 86, 248–255.
Griffin, W.L., Pearson, N.J., Belousova, E., Jackson, S.E., van Achterbergh, E., O'Reilly, S.Y., Shee, S.R., 2000. The Hf isotope composition of cratonic mantle: LAM-MC-ICPMS analysis of zircon megacrysts in kimberlites. Geochim. Cosmochim. Acta 64, 133–147.
Grimes, C.B., John, B.E., Cheadle, M.J., Mazdab, F.K., Wooden, J.L., Swapp, S., Schwartz, J.J., 2009. On the occurrence, trace element geochemistry, and crystallization history of zircon from in situ ocean lithosphere. Contrib. Miner. Petrol. 158, 757–783.
Hackspacher, P.C., Fetter, A.H., Ebert, H.D., Janasi, V.A., Dantas, E.L., Oliveira, M.A.F., Braga, I.F., Negri, F.A., 2003. Magmatismo há ca. 660–640 Ma no Domínio Socorro: registros de convergência pré-colisional na aglutinação do Gondwana Ocidental. Geologia USP, Série Científica 3, 85–96.
Hagen-Peter, G., Cottle, J.M., Tulloch, A.J., Cox, S.C., 2015. Mixing between enriched lithospheric mantle and crustal components in a short-lived subduction-related magma system, Dry Valleys area, Anatarctica: insights from U-Pb geochronology, Hf isotopes and whole-rock geochemistry. Lithosphere 7 (2), 174–188.
Hammarstrom, J.M., Zen, E.-An., 1986. Aluminium in hornblende: an empirical igneous geobarometer. Am. Mineral. 71, 1297–1313.
Harley, S.L., 1998. On the occurrence and characterization of ultrahigh-temperature crustal metamorphism. In: Treloar, P.J., O'Brien, P.J. (Eds.), What Drives Metamorphism and Metamorphic Reactions? Geological Society, London, Special Publication, pp. 81–107.
Harley, S.L., 2016. A matter of time: the importance of the duration of UHT metamorphism. J. Mineral. Petrol. Sci. 111, 50–72.
Harley, S.L., Kelly, N.M., Möller, A., 2007. Zircon and the thermal histories of hot mountain belts. Elements 3, 25–30.
Harley, S.L., Nandakumar, V., 2014. Accessory mineral behavior in granulite migmatites: A case study from the Kerala Khondalite Belt, India. J. Petrol. 55, 1965–2002.
Harrison, T.M., Watson, E.B., 1984. The behavior of apatite during crustal anatexis: equilibrium and kinetic considerations. Geochimica et Cosmochimica Acta 48, 1467–1477.
Henry, D.J., Guidotti, C.V., Thomson, J.A., 2005. The Ti-saturation surface for low-to-medium pressure metapelitic biotites: implications for geothermometry and Ti-substitution mechanisms. Am. Mineral. 90, 316–328.
Hermann, J., Müntener, O., Trommsdorff, V., Hansmann, W., Piccardo, G.B., 1997. Fossil crust-to-mantle transition, Val Malenco (Italian Alps). J. Geophys. Res. 102, 20123–20132.
Holland, T., Blundy, J., 1994. Non-ideal interactions in calcic amphiboles and their bearing on amphibole-plagioclase thermometry. Contrib. Miner. Petrol. 116, 433–447.
Hollister, L.S., Grissom, G.C., Peters, E.K., Stowell, H.H., Sisson, V.B., 1987. Confirmation of the empirical correlation of Al in hornblende with pressure of solidification of calc-alkaline plutons. Am. Mineral. 72, 231–239.
Jackson, S., Pearson, N.J., Griffin, W.L., Belousova, E.A., 2004. The application of laser ablation-inductively coupled plasma-mass spectrometry to in situ U-Pb zircon geochronology. Chem. Geol. 211, 47–69.
Janasi, V.A., 1999. Petrogênese de granitos crustais da Nappe de Empurrão Socorro-Guaxupé (SP-MG): uma contribuição da geoquímica elemental e isotópica. Thesis (Livre-Docência)—IGc-USP, 304 p.
Johnson, M.C., Rutherford, M.J., 1989. Experimental calibration of the aluminium-in-hornblende geobarometer with application to Long Valley Caldera (California) volcanic rocks. Geology 17, 837–841.
Kelly, N.M., Harley, S.L., 2004. Orthopyroxene–corundum in Mg–Al-rich granulites from the Oygarden Islands, East Antarctica. J. Petrol. 45 (7), 1481–1512.
Kelly, N.M., Harley, S.L., Möller, A., 2012. Complexity in the behavior and recrystallization of monazite during high-T metamorphism and fluid infiltration. Chem. Geol. 322–323, 192–208.
Kelsey, D.E., 2008. On ultrahigh-temperature crustal metamorphism. Gondwana Res. 13, 1–29.
Kelsey, D.E., Hand, M., 2015. On ultrahigh temperature crustal metamorphism: phase equilibria, trace element thermometry, bulk composition, heat sources, timescales and tectonic settings. Geosci. Front. 6, 311–356.
Kelsey, D.E., White, R.W., Holland, T.J.B., Powell, R., 2004. Calculated phase equilibria in K_2O-FeO-MgO-Al_2O_3-SiO_2-H_2O for sapphirine-quartz-bearing mineral assemblages. J. Metamorph. Geol. 22, 559–578.
Kemp, A.L.S., Slúmura, T., Hawkesworth, C.J., 2007. Linking granulites, silicic magmatism, and crustal growth in arcs: Ion microprobe (zircon) U-Pb ages from the Hidaka metamorphic belt, Japan. Geology 35, 807–810.
Kohn, M.J., Corrie, S.L., Markley, C., 2015. The fall and rise of metamorphic zircon. Am. Mineral. 100, 897–908.
Korhonen, F.J., Clark, C., Brown, M., Taylor, R.J.M., 2014. Taking the temperature of Earth's hottest crust. Earth Planet. Sci. Lett. 408, 341–354.
Kretz, R., 1982. Transfer and exchange equilibria in a portion of the pyroxene quadrilateral as deduced from natural and experimental data. Geochim. Cosmochim. Acta 46, 411–421.
Kunz, B.E., Regis, D., Engi, M., 2018. Zircon ages in granulite facies rocks: decoupling from geochemistry above 850 °C? Contrib. Mineral. Petrol. 173, 26. https://doi.org/10.1007/s00410-018-1454-5.
Lana, C., Farina, F., Gerdes, A., Alkmim, A., Gonçalves, G.O., Jardim, A.C., 2017.

Characterization of zircon reference materials via high precision U-Pb LA-MC-ICP-MS. J. Anal. Anat. Spectrom. 32, 2011–2023.
Lanari, P., Engi, M., 2017. Local bulk composition effects on mineral assemblages, in: Kohn, M.J., Engi, M., Lanari, P. (Eds.) Petrochronology. Reviews in Mineralogy and Geochemistry 83, pp. 55–102.
Lanari, P., Guillot, S., Schwartz, S., Vidal, O., Tricart, P., Riel, N., Beyssac, O., 2012. Diachronous evolution of the alpine continental subduction wedge: evidence from P-T estimates in the Briançonnais Zone houillere (France – Western Alps). J. Geodyn. 56–57, 39–54.
Lanari, P., Riel, N., Guillot, S., Vidal, O., Schwartz, S., Pêcher, A., Hattori, K.H., 2013. Deciphering high-pressure metamorphism in collisional context using microprobe mapping methods: application to the Stak eclogitic massif (northwest Himalaya). Geology 41 (2), 111–114. https://doi.org/10.1130/g33523.1.
Lanari, P., Vidal, O., De Andrade, V., Dubacq, B., Lewin, E., Grosch, E.G., Schwartz, S., 2014. XMapTools: a MATLAB©-based program for electron microprobe X-ray image processing and geothermobarometry. Comput. Geosci. 62, 227–240.
Lanari, P., Vho, A., Bovay, T., Airaghi, L., Centrella, S., 2018. Quantitative compositional mapping of mineral phases by electron probe micro-analyser. Geol. Soc. London Spec. Publ. 478https://doi.org/10.1144/SP478.4. SP478-4.
Larsen, E.S., 1929. The temperature of magmas. Am. Mineral. 14, 81–94.
Laurent, A., Bingen, B., Duchene, S., Whitehouse, M.J., Seydoux-Guillaume, A.-M., Bosse, V., 2018. Decoding a protracted zircon geochronological record in ultrahigh temperature granulite, and persistence of partial melting in the crust, Rogaland, Norway. Contrib. Mineral. Petrol. 173, 29. https://doi.org/10.1007/s00410-018-1455-4.
Laux, J.H., Pimentel, M.M., Dantas, E.L., Armstrong, R., Junges, S.L., 2005. Two Neoproterozoic custal accretion events in the Brasília Belt, central Brazil. J. S. Am. Earth Sci. 18, 183–198.
Liang, Y., Sun, C.G., Yao, L.J., 2013. A REE-in-two-pyroxene thermometer for mafic and ultramafic rocks. Geochim. Cosmochim. Acta 102, 246–260.
Ludwig, K.R., 2003. Isoplot Excell version 3.0. A geochronological toolkit for Microsoft Excel, Berkeley Geochronological Centre Special Publication No. 4, Berkeley, California.
Mantovani, M.S.M., Brito-Neves, B.B., 2005. The Paranapanema lithospheric block: its importance for Proterozoic (Rodinia, Gondwana) supercontinent theories. Gondwana Res. 8 (3), 303–315.
Mantovani, M.S.M., Brito-Neves, B.B., 2009. 2009. The Paranapanema Lithospheric Block: its nature and role in the Accretion of Gondwana. In: Gaucher, C., Sial, A., Halverson, G., Frimmel, H. (Eds.), Neoproterozoic-Cambrian Tectonics, Global Change and Evolution: A Focus on South Western Gondwana. Elsevier, Amsterdam, pp. 257–272.
McDonough, W.F., Sun, S.S., 1995. The composition of the earth. Chem. Geol. 120, 223–254.
Melo, M., Lana, C., Stevens, G., Pedrosa-Soares, A., Gerdes, A., Alkmin, A., Nalini Jr., H., Alkmim, F., 2017. Assessing the isotopic evolution of S-type granites of the Carlos Chagas Batholith, SE Brazil: Clues from U-Pb, Hf isotopes, Ti geothermometry and trace element composition of zircon. Lithos 284–285, 730–750.
Möller, A., O′ Brien, P.J., Kennedy, A., Kröner, A., 2003. Linking growth episodes of zircon and metamorphic textures to zircon chemistry: an example from the ultrahigh temperature granulites of Rogaland (SW Norway). In: Vance, D., Müller, W., I.M, Villa (Eds.), Geochronology: Linking the Isotopic Record with Petrology and Textures—Geological Society, London, Special Publications 220, pp. 65–81.
Mora, C.A.S., Campos Neto, M.C., Basei, M.A.S., 2014. Syn-collisional lower continental crust anataxis in the Neoproterozoic Socorro-Guaxupé Nappe System, southern Brasília Orogen, Brazil: constraints from zircon U-Pb dating, Sr-Nd-Hf signatures and whole-rock geochemistry. Precambr. Res. 255, 847–864.
Moraes, R., Fuck, R.A., 2000. Ultra-high-temperature metamorphism in Central Brazil: the Barro Alto complex. J. Metamorph. Geol. 18, 345–358.
Morel, M.L.A., Nebel, O., Nebel-Jacobsen, Y.J., Miller, J.S., Vroon, P.Z., 2008. Hafnium isotope characterization of the GJ-1 zircon reference material by solution and laser-ablation MC-ICPMS. Chem. Geol. 255, 231–235.
Pearce, J.A., Harris, N.B.W., Tindle, A.G., 1984. Trace element discrimination diagramsfor the tectonic interpretation of granitic rocks. J. Petrol. 25, 956–983.
Peixoto, E.I.P., Falci, A., Noronha, R.C., Degler, R., Martins, L.C.D., Nassif, M.T., Freitas, A.R., Novo, T., 2015. Geologia das Folhas Andradas (SF.23-Y-A-III) e Ouro Fino 1:100.000 (SF.23-Y-B-I). Projeto Fronteiras de Minas, CODEMIG-UFMG, Belo Horizonte, Brazil.
Pimentel, M.M., 2016. The tectonic evolution of the Neoproterozoic Brasília Belt, central Brazil: a geochronological and isotopic approach. Braz. J. Geol. 46 (1), 67–82.
Pimentel, M.M., Fuck, R.A., 1992. Neoproterozoic crustal accretion in central Brazil. Geology 20, 375–379.
Pimentel, M.M., Fuck, R.A., Gioia, D.M.C.L., 2000. The Neoproterozoic Goiás Magmatic Arc, Central Brazil: a review and new Sm-Nd isotopic data. Revista Brasileira de Geociências 30 (1), 35–39.
Reno, B.L., Brown, M., Kobayashi, K., Nakamura, E., Piccoli, P.M., Trouw, R.A.J., 2009. Eclogite-high-pressure granulite metamorphism records early collision in west gondwana: new data from the southern brasília belt, Brazil. J. Geol. Soc., London 166, 1013–1032. https://doi.org/10.1144/0016-76492008-140.
Reno, B.L., Piccoli, P.M., Brown, M., Trouw, R.A.J., 2012. In situ monazite (U–Th)–Pb ages from the Southern Brasília Belt, Brazil: constraints on the high temperature retrograde evolution of HP granulites. J. Metamorph. Geol. 30 (1), 81–112.
Ribeiro, A., Nascimento, D., Bongiolo, E., Trouw, R., Polo, H., Tavares, F., Nepomuceno, F., 2015a. Geologia da Folha Pouso Alegre (SF.23-Y-B-II) 1:100.000. Programa Geologia do Brasil, CPRM-UFRJ, Rio de Janeiro, Brazil.
Ribeiro, A., Nascimento, D., Campos, M.T., Oliveira, F., Rocha, F., 2015b. Geologia da Folha Machado (SF.23-V-D-V) 1:100.000. Programa Geologia do Brasil, CPRM-UFRJ, Rio de Janeiro, Brazil.
Ribeiro, A., Campos, M.T., Paciullo, F.V., Carvalho, M.V., Valeriano, C.M., Nascimento, D., 2015c. Geologia da Folha Alfenas (SF.23-V-D-II) 1:100.000. Programa Geologia do Brasil, CPRM-UFRJ, Rio de Janeiro, Brazil.
Rocha, B.C., Moraes, R., Möller, A., Cioffi, C.R., Jercinovic, M.J., 2017. Timing of anatexis and melt crystallization in the Socorro-Guaxupé Nappe, SE Brazil: insights from trace element composition of zircon, monazite and garnet coupled to U-Pb geochronology. Lithos 277, 337–355.
Rocha, B.C., Moraes, R., Möller, A., Cioffi, C.R., 2018. Magmatic inheritance vs. UHT metamorphism: zircon petrochronology of granulites and petrogenesis of charnockitic leucosomes of the Socorro-Guaxupé Nappe, SE Brazil. Lithos 314–315, 16–39. https://doi.org/10.1016/j.lithos.2018.05.014.
Rocha, B.C. 2016. Idade, duração e condições P-T do metamorfismo de temperatura ultra-alta, anatexia e cristalização de fundido na nappe Socorro-Guaxupé. PhD thesis, Universidade de São Paulo, p. 229.
Rubatto, D., 2002. Zircon trace element geochemistry: distribution coefficients and the link between U-Pb ages and metamorphism. Chem. Geol. 184, 123–138.
Rubatto, D., 2017. Zircon: The Metamorphic Mineral, In: Kohn, M.J., Engi, M., Lanari, P. (Eds.) Petrochronology. Reviews in Mineralogy and Geochemistry 83, pp. 261–289.
Rubatto, D., Williams, I.S., Buick, I.S., 2001. Zircon and monazite response to prograde metamorphism in the Reynolds Range, central Australia. Contrib. Miner. Petrol. 140, 458–468.
Rubatto, D., Chakraborty, S., Dasgupta, S., 2013. Timescales of crustal melting in the Higher Himalayan Crystallines (Sikkim, Eastern Himalaya) inferred from trace element-constrained monazite and zircon chronology. Contrib. Mineral. Petrol. 165 (2), 349–372.
Santos, M.M., Lana, C., Scholz, R., Buick, I., Schmitz, M.D., Kamo, S.L., Gerdes, A., Corfu, F., Tapster, S., Lancaster, P., Storey, C.D., Basei, M.A.S., Tohver, E., Alkmim, A., Nalini, H., Krambrock, K., Fantini, C., 2017. A new appraisal of Sri Lankan zircons as reference material for in situ U-Pb geochronology, REE analyses and Lu-Hf isotope tracing. Geostand. Geoanal. Res. J. 41 (3), 335–358.
Santosh, M., Tsunogae, T., Li, J.H., Liu, S.J., 2007. Discovery of sapphirine-bearing Mg-Al granulites in the North China Craton: implications for Palaeoproterozoic ultrahigh temperature metamorphism. Gondwana Res. 11, 263–285.
Sawyer, E.W., 1987. The role of partial melting and fractional crystallization in determining discordant migmatite leucosome compositions. J. Petrol. 32, 701–738.
Sawyer, E.W., 1999. Criteria for the recognition of partial melting. Phys. Abd Chem. Earth, Part A: Solid Earth Geod. 24 (3), 269–279.
Sawyer, E.W., 2008. The Atlas of migmatites. The Canadian Mineralogist, Special Publication 9. NRC Research Press, Ottawa, pp. 371.
Slama, J., Kosler, J., Condon, D.J., Crowley, J.L., Gerdes, A., Hanchar, J.M., Horstwood, M.S.A., Morris, G.A., Nasdala, L., Norberg, N., Schaltegger, U., Schoene, B., Tubrett, M.N., Whitehouse, M.J., 2008. Plesovice zircon – a newnatural reference material for U-Pb and Hf isotopic microanalysis. Chem. Geol. 249, 1–35.
Spear, F.S., Pyle, J.M., 2010. Theoretical modeling of monazite growth in a low-Ca metapelite. Chem. Geol. 273 (1–2), 111–119.
Stepanov, A., Rubatto, D., Hermann, J., Korsakov, A.V., 2016. Contrasting P-T paths within the Barchi-Kol UHP terrain (Kokchetav Complex): Implications for subduction and exhumation of continental crust. Am. Mineral. 101 (4), 788–807.
Sun, C.G., Liang, Y., 2015. A REE-in-garnet–clinopyroxene thermobarometer for eclogites, granulites and garnet peridotites. Chem. Geol. 393–394, 79–92.
Taylor, R.J.M., Kirkland, C.L., Clark, C., 2016. Accessories after the facts: Constraining the timing, duration and conditions of high-temperature metamorphic processes. Lithos 264, 239–257.
Tedeschi, M., Novo, T., Azevedo, R., Amaral, L.F.S., Degler, R., Viera, P.L.N.C.R., 2015. Geologia das Folha Caldas (SF.23-V-D-IV) e Poços de Caldas (SF.23-V-C-VI) 1:100.000. Projeto Fronteiras de Minas, CODEMIG-UFMG, Belo Horizonte, Brazil.
Tedeschi, M., Lanari, P., Rubatto, D., Pedrosa-Soares, A., Hermann, J., Dussin, I., Pinheiro, M.A.P., Bouvier, A.-S., Baumgartner, L., 2017. Reconstruction of multiple P-T-t stages from retrogressed mafic rocks: Subduction versus collision in the Southern Brasília orogen (SE Brazil). Lithos 294–295, 283–303.
Thorpe, R.S., Francis, P.W., Harmon, R.S., 1981. Andean andesites and crustal growth. Philos. Trans. Royal Soc. London 301, 305–320.
Töpfner, C., 1996. Brasiliano-granitoide in den Bundesstaaten São Paulo und Minas Gerais, Brasilieneine Vergleichende studie. Münchner Geologische Hefte A17, 258.
Trouw, R.A.J., Heilbron, M., Ribeiro, A., Paciullo, F., Valeriano, C.M., Almeida, J.C.H., Tupinambá, M., Andreis, R.R., 2000. The central segment of Ribeira belt. In: Cordani, U.G., Milani, E.J., Thomaz Filho, A., Campos, D.A. (Eds.), Tectonic Evolution of South America. 31th International Geological Congress. Rio de Janeiro, Brazil, pp. 287–310.
Trouw, R.A.J., Nunes, R.P.M., Castro, E.M.O., Trouw, C.C., Matos, G.C., 2008. Nota explicativa das Folhas Varginha (SF.23-V-D-VI) e Itajubá (SF.23-Y-B-III). Programa Geologia do Brasil. Contrato CPRM-UFRJ, p. 99.
Trouw, R.A.J., Peternel, R., Ribeiro, A., Heilbron, M., Vinagre, R., Duffles, P., Trouw, C.C., Fontainha, M., Kussama, H.H., 2013. A new interpretation for the interference zone between the southern Brasília belt and the central Ribeira belt, SE Brazil. J. S. Am. Earth Sci. 48, 43–57.
Trouw, C.C., 2008. Mapeamento da Folha Virgínia–MG, Geocronologia U-Pb (SHRIMP) em zircões e interpretação geotectônica. PhD Thesis, Universidade do Rio de Janeiro, p.127.
Valeriano, C., 2017. The Southern Brasília Belt. In: Heilbron, M., Cordani, U.G., Alkmim, F.F. (Eds.), São Francisco Craton, Eastern Brazil. Springer International Publishing, Switzerland, pp. 189–205.
Valley, P.M., Fisher, C.M., Hanchar, J.M., Lam, R., Tubrett, M., 2010. Hafnium isotopes in zircon: A tracer of fluid-rock interaction during magnetite–apatite (“Kiruna-type”) mineralization. Chem. Geol. 275, 208–220.
Van Achterbergh, E., Ryan, C.G., Jackson, S.E., Griffin, W.L., 2001. Data reduction software for LA-ICP-MS: appendix. In: Sylvester P.J. (Eds.), Laser Ablation-ICPMass

Spectrometry in the Earth Sciences: Principles and Applications, Ottawa, Mineralogical Association Canada (MAC) Short Course Series 29, 239–243.
Vermeesch, P., 2012. On the visualisation of detrital age distributions. Chem. Geol. 312–313, 190–194.
Vervoort, J.D., Kemp, A.I.S., 2016. Clarifying the zircon Hf isotope record of crust–mantle evolution. Chem. Geol. 425, 65–75.
Vinagre, R., Trouw, R.A.J., Mendes, J.C., Duffles, P., Peternel, R., Matos, G., 2014. New Evidence of a Magmatic Arc in the Southern Brasília Belt, Brazil: The Serra da Água Limpa Batholith (Socorro-Guaxupé Nappe). J. South Am. Earth Sci. 54, 120–139.
Vinagre, da C.R., Trouw, R.A.J., Mendes, J.C., Geraldes, M., Távora, A., Nepomuceno, F., Barros Jr., E.A., 2017. Proterozoic evolution of part of the Embu Complex, eastern São Paulo state, SE Brazil. J. South Am. Earth Sci. 79, 170–188.
Wang, W., Liu, S., Cawood, P.A., Guo, Rongrong, Bai, X., Guo, B., 2017. Late Neoarchean crust-mantle geodynamics: evidence from Pingquan Complex of the -Northern Hebei Province, North China Craton. Precambrian Res. 303, 473–493.
Wasserburg, G.J., 1963. Diffusion processes in lead-uranium systems. J. Geophys. Res. 68, 4823–4846.
Watson, E.B., Harrison, T.M., 1983. Zircon saturation revisited: temperature and composition effects in a variety of crustal magma types. Earth Planet. Sci. Lett. 64, 295–304.
Watson, E.B., Wark, D.A., Thomas, J.B., 2006. Crystallization thermometers for zircon and rutile. Contrib. Mineral. Petrol. 151, 413–433.
Westin, A., Campos Neto, M.C., Hawkesworth, C.J., Cawood, P.A., Dhuime, B., Delavault, H., 2016. A Paleoproterozoic intra-arc basin associated with a juvenile source in the Southern Brasilia Orogen: Application of U-Pb and Hf–Nd isotopic analyses to provenance studies of complex areas. Precambr. Res. 276, 178–193.
Whitehouse, M., Kemp, A.I.S., 2010. On the difficulty of assigning crustal residence, magmatic protolith and metamorphic ages to Lewisian granulites: constraints from combined in situ U-Pb and Lu–Hf isotopes. Geol. Soc., London, Spec. Publ. 335, 81–101.
Whitney, D.L., Evans, B.W., 2010. Abbreviations for names of rock-forming minerals. Am. Mineral. 95, 185–187.
Wiedenbeck, M., Alle, P., Corfu, F., Griffin, W.L., Meier, M., Oberli, F., Von Quadt, A., Roddick, J.C., Spiegel, W., 1995. 3 natural zircon standards for U-Th-Pb, Lu-Hf, trace-element and REE analyses. Geostand. Newsl. 19, 1–23.
Yakymchuk, C., 2017. Behaviour of apatite during partial melting of metapelites and consequences for prograde suprasolidus monazite growth. Lithos 274–275, 412–426.
Yang, C., Wei, C., 2017. Ultrahigh temperature (UHT) mafic granulites in the East Hebei, North China Craton: Constraints from a comparison between temperatures derived from REE-based thermometers and major element-based thermometers. Gondwana Research 46, 156–169.
Zeh, A., Gerdes, A., Will, T.M., Frimmel, H.E., 2010. Hafnium isotope homogenization during metamorphic zircon growth in amphibolite-facies rocks: examples from the Shackleton Range (Antarctica). Geochimica et Cosmochimica Acta 74 (16), 4740–4758.
Zheng, Y.F., Wu, Y.-B., Zhao, Z.-F., Zhang, S.-B., Xu, P., Wu, F.-Y., 2005. Metamorphic effect on zircon Lu–Hf and U-Pb isotope systems in ultrahigh-pressure eclogite-facies metagranite and metabasalt. Earth Planet. Sci. Lett. 240, 378–400.
Zogheib, F.F., Degler, R., Martins, L.C.D., Novo, T., 2015. Geologia das Folha Guaxupé (SF.23-V-C-III) 1:100.000. Projeto Fronteiras de Minas, CODEMIG-UFMG, Belo Horizonte, Brazil.